



HAL
open science

Coupled retrieval of aerosol properties and land surface reflection using the Airborne Multiangle SpectroPolarimetric Imager

Feng Xu, Gerard van Harten, David J. Diner, Olga V. Kalashnikova, Felix C. Seidel, Carol J. Bruegge, Oleg Dubovik

► **To cite this version:**

Feng Xu, Gerard van Harten, David J. Diner, Olga V. Kalashnikova, Felix C. Seidel, et al.. Coupled retrieval of aerosol properties and land surface reflection using the Airborne Multiangle SpectroPolarimetric Imager. *Journal of Geophysical Research: Atmospheres*, 2017, 122, pp.7004-7026. 10.1002/2017JD026776 . insu-03686238

HAL Id: insu-03686238

<https://insu.hal.science/insu-03686238>

Submitted on 2 Jun 2022

HAL is a multi-disciplinary open access archive for the deposit and dissemination of scientific research documents, whether they are published or not. The documents may come from teaching and research institutions in France or abroad, or from public or private research centers.

L'archive ouverte pluridisciplinaire **HAL**, est destinée au dépôt et à la diffusion de documents scientifiques de niveau recherche, publiés ou non, émanant des établissements d'enseignement et de recherche français ou étrangers, des laboratoires publics ou privés.

Copyright

RESEARCH ARTICLE

10.1002/2017JD026776

Key Points:

- An reliable retrieval algorithm has been developed for simultaneous retrieval of aerosol properties and surface reflection using AirMSPI
- We identify the best angular combinations for multiangle observations from the retrieval quality assessment
- We explore the benefits of polarimetric and multiangular measurements and target revisits in constraining aerosol and surface retrieval

Correspondence to:

F. Xu,
feng.xu@jpl.nasa.gov

Citation:

Xu, F., G. van Harten, D. J. Diner, O. V. Kalashnikova, F. C. Seidel, C. J. Bruegge, and O. Dubovik (2017), Coupled retrieval of aerosol properties and land surface reflection using the Airborne Multiangle SpectroPolarimetric Imager, *J. Geophys. Res. Atmos.*, 122, 7004–7026, doi:10.1002/2017JD026776.

Received 10 MAR 2017

Accepted 9 JUN 2017

Accepted article online 11 JUN 2017

Published online 6 JUL 2017

Coupled retrieval of aerosol properties and land surface reflection using the Airborne Multiangle SpectroPolarimetric Imager

Feng Xu¹ , Gerard van Harten¹, David J. Diner¹ , Olga V. Kalashnikova¹, Felix C. Seidel¹ , Carol J. Bruegge¹, and Oleg Dubovik²

¹Jet Propulsion Laboratory, California Institute of Technology, Pasadena, California, USA, ²Laboratoire d'Optique Atmosphérique, UMR8518 CNRS/Université Lille-1, Villeneuve-d'Ascq, France

Abstract The Airborne Multiangle SpectroPolarimetric Imager (AirMSPI) has been flying aboard the NASA ER-2 high-altitude aircraft since October 2010. In step-and-stare operation mode, AirMSPI acquires radiance and polarization data in bands centered at 355, 380, 445, 470*, 555, 660*, 865*, and 935 nm (* denotes polarimetric bands). The imaged area covers about 10 km by 11 km and is typically observed from nine viewing angles between $\pm 66^\circ$ off nadir. For a simultaneous retrieval of aerosol properties and surface reflection using AirMSPI, an efficient and flexible retrieval algorithm has been developed. It imposes multiple types of physical constraints on spectral and spatial variations of aerosol properties as well as spectral and temporal variations of surface reflection. Retrieval uncertainty is formulated by accounting for both instrumental errors and physical constraints. A hybrid Markov-chain/adding-doubling radiative transfer (RT) model is developed to combine the computational strengths of these two methods in modeling polarized RT in vertically inhomogeneous and homogeneous media, respectively. Our retrieval approach is tested using 27 AirMSPI data sets with low to moderately high aerosol loadings, acquired during four NASA field campaigns plus one AirMSPI preengineering test flight. The retrieval results including aerosol optical depth, single-scattering albedo, aerosol size and refractive index are compared with Aerosol Robotic Network reference data. We identify the best angular combinations for 2, 3, 5, and 7 angle observations from the retrieval quality assessment of various angular combinations. We also explore the benefits of polarimetric and multiangular measurements and target revisits in constraining aerosol property and surface reflection retrieval.

1. Introduction

Aerosols, airborne suspensions of tiny particles, are major components of Earth's climate system. They scatter and absorb sunlight to varying degrees and have major influences on Earth's energy and water cycles. Over populated areas, aerosols also impact public health as the fine particles penetrate deep into human lungs and carry toxins into our bloodstreams while coarse particles irritate and inflame our respiratory systems. Quantification of these effects requires accurate characterization of aerosol abundances, optical properties, and microphysical properties including size, shape, and composition. Compared to current generations of radiometric single-angle remote sensors (e.g., the Moderate Resolution Imaging Spectroradiometer, MODIS) [Salomonson *et al.*, 1989; King *et al.*, 1992], multiangular imagers (e.g., the Multiangle Imaging SpectroRadiometer, MISR) [Diner *et al.*, 1998] improve sensitivity to aerosol microphysical properties [Kahn and Gaitley, 2015]. Moreover, many sensitivity studies and real data analyses indicate that both ground-borne and spaceborne remote sensing of aerosols can be further enhanced by incorporating polarization into the measurements [e.g., Mishchenko and Travis, 1997; Hasekamp, 2010; Lebsack *et al.*, 2007; Xu and Wang, 2015, among others].

A number of spaceborne and airborne passive remote sensors with multiangular, multispectral, and polarimetric capabilities have been developed for passive aerosol remote sensing. These include the satellite Polarization and Directionality of Earth's Reflectances (POLDER) [Deschamps *et al.*, 1994] which acquires up to 16 viewing directions in six aerosol bands from visible to near infrared with ~ 6 km spatial resolution at nadir. Airborne instruments include the Research Scanning Polarimeter (RSP) [Cairns *et al.*, 1999], a nonimaging scanner that provides ~ 152 different viewing angles within $\pm 60^\circ$ along track in nine spectral bands; the airborne Spectropolarimeter for Planetary Exploration instrument [Rietjens *et al.*, 2015], a hyperspectral

polarimetric sensor with a radiometric spectral resolution of ~ 1 nm and polarimetric spectral resolution of 10–20 nm (depending on wavelength); and the Passive Aerosol and Cloud Suite polarimeter, which covers a 110° cross-track field of view with hyperangular imaging coverage between $\pm 55^\circ$ along track [Martins *et al.*, 2013]. At JPL, the Airborne Multiangle SpectroPolarimetric Imager (AirMSPI) [Diner *et al.*, 2013] is an eight-band (ultraviolet-visible near-infrared) pushbroom camera mounted on a gimbal to acquire programmable multiangular observations over a $\pm 66^\circ$ along-track range in step-and-stare operation mode, with 10 m resolution over a 10 km by 11 km imaged area. The Stokes vector components Q and U of scattered light are measured in the 470, 660, and 865 nm bands by using a dual photoelastic modulator-based polarimetric imaging approach [Diner *et al.*, 2007].

A reliable aerosol retrieval algorithm that takes full advantage of the multidimensional measurements acquired by such instruments is required. Many aerosol retrieval algorithms rely on the lookup table (LUT) method, whereby precalculated radiances for a set of properly selected aerosol models are compared to the observations and those with lowest-fitting residues are selected as solutions. For example, the MISR retrievals use a LUT containing 74 aerosol mixtures [Kahn *et al.*, 2010]. The main disadvantage of LUT approach is that the predetermined aerosol models might not fully represent the global and temporal variations of aerosol properties found in nature, and lack of the correct model can bias the retrievals [Diner *et al.*, 2011]. To overcome this limitation, various types of optimization algorithms have been developed [cf. reviews in Dubovik [2004] and Kokhanovsky [2015], among others]. Their main features include (a) a compact and continuous representation of the relevant parameter space; (b) an imposition of both observational and physical constraints to stabilize the retrieval and enhance its accuracy; and (c) flexibility for including multiple parameters to represent aerosol properties and surface reflection.

The multipixel aerosol retrieval algorithm [Dubovik *et al.*, 2011] is one of the most recently developed optimization approaches. It integrates multispectral, multiangular, and polarimetric observations along with physical constraints in the spatial, spectral, and temporal dimensions regarding smooth variations of certain aerosol and/or surface reflection properties. Complementary to the implementation of the multipixel algorithm to retrieve satellite-borne POLDER observations, we adapt a similar algorithm to airborne remote sensing observations by AirMSPI. Moreover, we incorporate a methodology to estimate the aerosol and surface reflection retrieval uncertainties by accounting for both instrumental errors and the abovementioned physical constraints. Note that the “multipixel” approach, which involves spatial regularization of the retrieved aerosol fields, is instead referred to as “multipatch” in the current paper to avoid confusion with three-dimensional radiative transfer (RT) models that account for propagation of photons in the horizontal direction. Indeed, our model is a one-dimensional (1-D) code based on the independent pixel approximation [Cahalan *et al.*, 1994] to ensure forward modeling efficiency. We use this algorithm to explore the benefits of multiangle radiometry and polarimetry and the importance of target revisits for surface reflection and aerosol property characterization. A hybrid RT model (Markov chain/adding-doubling or “MarCh-AD”) is established to combine the strengths of these two methods to enable efficient forward RT modeling and Jacobian evaluation for the coupled atmosphere-surface system (CASS).

The paper is organized as follows. Following an algorithm overview in section 2, we introduce our RT model for polarized RT in CASS in section 3. The multipatch retrieval algorithm and error analysis formalism are described in section 4. In section 5, the retrieval algorithm is tested using 27 AirMSPI data sets acquired during the Polarimeter Definition Experiment (PODEX), Studies of Emissions, Atmospheric Composition, Clouds and Climate Coupling by Regional Surveys (SEAC⁴RS), the Precipitation, Aerosols, and Pacific Atmospheric Rivers Experiment (CalWater-2), Imaging Polarimetric Assessment and Characterization of Tropospheric Particulate Matter (ImPACT-PM) field campaigns plus one AirMSPI preengineering test flight, with aerosol loadings ranging from low to moderately high. By the use of these AirMSPI observations, the benefits of multiangle polarimetric measurements and target revisits on constraining aerosol and surface retrieval are investigated. A summary is presented in section 6.

2. General Structure of the Algorithm

An overview of coupled retrieval of aerosol properties and surface reflection algorithm flow is given in Figure 1. The aerosol microphysical properties include spectrally dependent real and imaginary parts of aerosol refractive index, volume concentrations of all aerosol size components, and nonspherical particle fraction.

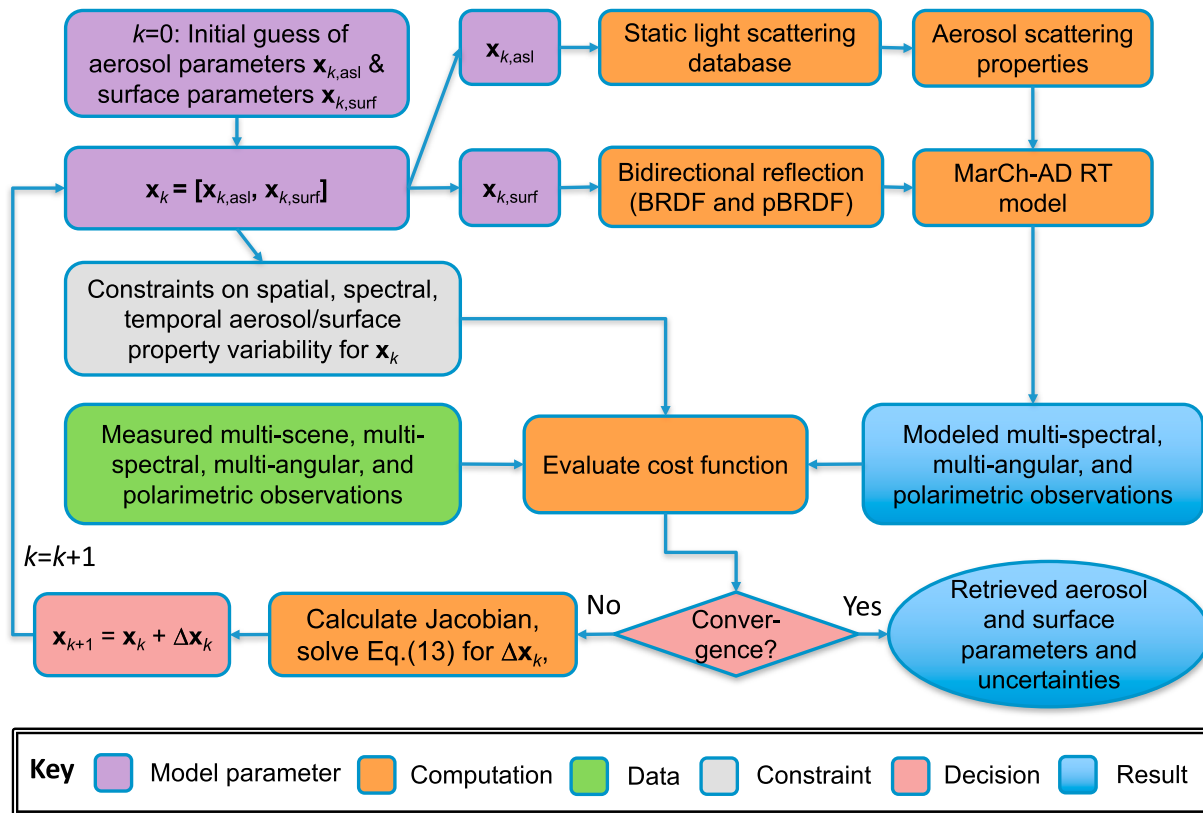


Figure 1. Algorithm flowchart for coupled retrieval of aerosol land surface reflection properties.

These are input to a Mie scattering (or for the nonspherical component, a spheroidal particle scattering) database for determining aerosol optical properties via interpolation [Dubovik et al., 2011; Xu et al., 2016]. The modeled optical properties include aerosol optical depth (AOD), single-scattering albedo (SSA), and phase matrix. Further assuming a Gaussian profile for the aerosol vertical distribution characterized by a mean height and a standard deviation (cf. section 3.1), the overall optical properties of mixed aerosol/Rayleigh sublayers are determined. The surface parameters include spectral weight and angular shape parameters for unpolarized surface reflection, and spectral weight, shadowing width, and slope variance of microfacets for the polarized component (cf. section 3.2). With the surface reflection and aerosol/Rayleigh optical properties, a hybrid RT model that couples Markov chain and doubling-adding methods is used to model radiance and polarization. Our algorithm builds upon the concept of multipatch regularization with convergence and robustness ensured by imposing constraints on (a) the spectral variation of aerosol optical properties and a set of surface parameters, (b) the spatial variation of aerosol parameters across neighboring image pixels, and (c) temporal variations of surface reflection properties (cf. section 4.1). The set of parameters in the highly nonlinear system is solved iteratively. Iterations repeat until convergence is achieved or a specified maximum number of iterations occur.

The retrieval output includes all above mentioned aerosol and surface parameters, including aerosol loading and microphysical properties from which AOD and SSA are determined, aerosol distribution profile, and surface parameters from which surface albedo is calculated. Retrieval uncertainties in these parameters are also obtained.

3. Radiative Transfer in the Coupled Atmosphere-Surface System

As illustrated in Figure 2, a multilayer coupled atmosphere-surface system (CASS) consisting (from the bottom up) of the land surface, a pure Rayleigh layer, and an aerosol/Rayleigh mixed layer is established.

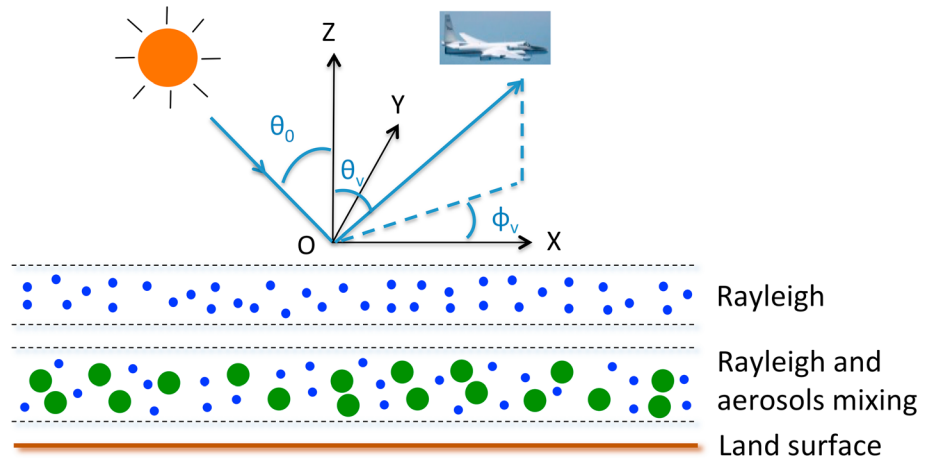


Figure 2. Depiction of the multilayer CASS model. The Sun illuminates the top of atmosphere with solar zenith angle θ_0 in the principal plane O-XZ. The sensor views the atmosphere at viewing angle θ_v and azimuthal angle ϕ_v . A Gaussian vertical distribution profile for aerosols is assumed in the aerosol/Rayleigh mixed layer, and the Markov chain model is used for computing polarized RT in this layer. The Rayleigh layer is optically homogeneous, and the doubling method is used for RT modeling. Coupling of local radiative fields between these layers and inclusion of the land surface is completed by using an adding strategy.

The Rayleigh layer is optically homogeneous while the “mixed layer” is inhomogeneous as the aerosol has its own vertical distribution profile different than that of the Rayleigh-scattering molecular atmosphere.

3.1. Aerosol Profile and Size Distribution

The vertically inhomogeneous aerosol/Rayleigh mixed layer is assumed to have a minimum altitude h_{\min} and a maximum altitude h_{\max} and is divided into a set of sublayers to facilitate evaluation of the optical properties used in the polarized RT modeling. Aerosols are distributed throughout the mixed layer with an assumed Gaussian profile characterized by mean height h_a and standard deviation σ_a . Then, the aerosol concentration profile c_a as a function of altitude h is

$$c_a(h) = \frac{\sqrt{\pi}\sigma_a}{2} \left[\operatorname{erf}\left(\frac{h_{\max} - h_a}{\sigma_a}\right) - \operatorname{erf}\left(\frac{h_{\min} - h_a}{\sigma_a}\right) \right] \exp\left[-\frac{(h - h_a)^2}{\sigma_a^2}\right], \quad (1)$$

where $\operatorname{erf}(x)$ is the error function.

The aerosol size distribution is composed of N_{sc} lognormal volume-weighted components, each parameterized by a median radius $r_{m,i}$ and a standard deviation σ_i , namely,

$$\frac{dV(r)}{d \ln r} = \sum_{k=1}^{N_{sc}} C_{v,k} \frac{1}{\sqrt{2\pi}\sigma_k} \exp\left[-\frac{(\ln r - \ln r_{m,k})^2}{2\sigma_k^2}\right], \quad (2)$$

Table 1. Median Radius (r_m) and Standard Deviation (σ) of $N_{sc} = 5$ Volume Weighted Lognormal Size Components for Aerosol Over Land Retrieval

Bin Number	Median Radius (r_m , μm)	Standard Deviation (σ)
1	0.13	0.35
2	0.20	0.35
3	0.33	0.35
4	1.03	0.5
5	2.93	0.5

where $C_{v,k}$ are the column volume concentration of the k th aerosol size component, respectively, and is related to its volume fraction (f_k) in the total volume concentration ($C_{v, \text{tot}}$) by $C_{v,k} = C_{v, \text{tot}} f_k$ where $C_{v, \text{tot}}$ is the total volume concentration $C_{v, \text{tot}} = C_{v, 1} + C_{v, 2} + C_{v, 3} + \dots$. As parameterized in Table 1, five aerosol size components ($N_{sc} = 5$ in

equation (2)) are used in our current work to constitute the size distribution. Their concentrations $C_{v,k}$ are determined from optimization. Together with the aerosol refractive index ($m = m_r + im_i$) concentration profile, volume fraction (f_{ns}) of nonspherical particles (modeled by spheroids [Dubovik et al., 2006] as well as the Rayleigh profile, the optical depth, single-scattering albedo, and phase matrices of all sublayers are evaluated [Xu et al., 2016] and then used for RT modeling (cf. section 3.3).

3.2. Surface Reflection

The surface reflectance function has two components: the bidirectional reflectance distribution function (BRDF) parameterized by the Rahman-Pinty-Verstraete (RPV) model [Rahman et al., 1993] and the polarized BRDF (pBRDF) parameterized by a microfacet model [Litvinov et al., 2011]. Accounting for both terms, the overall surface reflection matrix \mathbf{R}_{surf} is expressed as

$$\begin{aligned} \pi \mathbf{R}_{\text{surf}} = & a_\lambda \frac{(\cos \theta_0 \cos \theta_v)^{k_\lambda - 1}}{(\cos \theta_0 + \cos \theta_v)^{1 - k_\lambda}} F(g_\lambda; \Omega) [1 + R(G)] \mathbf{D} \\ & + \varepsilon_\lambda \frac{\mathbf{r}(\pi - i_2) \mathbf{F}_p(n_{\text{surf}}; \Omega) \mathbf{r}(-i_1)}{4\mu_n^A (\cos \theta_0 + \cos \theta_v)} \frac{1}{2\sigma_s^2} \exp\left(-\frac{1 - \mu_n^2}{\mu_n^2 2\sigma_s^2}\right) f_{\text{sh}}(\Omega), \end{aligned} \quad (3)$$

with \mathbf{D} being the null matrix except $D_{11} = 1$. Denoting (θ_0, ϕ_0) and (θ_v, ϕ_v) as the combinations of zenith angles and azimuthal angles of the incident and viewed light, respectively, the scattering angle is calculated by

$$\cos \Omega = -\mu_v \mu_0 + \sqrt{1 - \mu_v^2} \sqrt{1 - \mu_0^2} \cos(\phi_v - \phi_0), \quad (4)$$

where μ_0 and μ_v are the cosines of θ_0 and θ_v , respectively.

The first part on the right-hand side of equation (3) is the RPV model characterizing the unpolarized surface reflection: with a_λ controlling the amplitude of reflection ($0 < a_\lambda < 1$) and the modified Minnaert term k_λ dominating the bowl or bell shape of the angular distribution ($-1 < k_\lambda < 1$) and g_λ is the asymmetry parameter of the Henyey-Greenstein phase function ($-1 < g_\lambda < 1$) so that $F(g_\lambda; \Omega)$ expressed as

$$F(g_\lambda; \Omega) = \frac{1 - g_\lambda^2}{(1 + g_\lambda^2 - 2g_\lambda \cos \Omega)^{3/2}}, \quad (5)$$

and to account for the “hot spot” effect, $1 + R(G)$ is used where

$$R(G) = \frac{1 - a_\lambda}{1 + G}, \quad (6)$$

with

$$G = \sqrt{\tan^2 \theta_0 + \tan^2 \theta_v - 2 \tan \theta_0 \tan \theta_v \cos(\phi_v - \phi_0)}. \quad (7)$$

The second part of equation (3) describes the polarized component of the surface reflection: the matrices $\mathbf{r}(\pi - i_2)$ and $\mathbf{r}(i_1)$ rotate the Stokes vector into the meridian and reflection planes via angles

i_1 and i_2 , respectively [Hovenier, 1969]; \mathbf{F}_p is the Fresnel reflection matrix as a function of surface refractive index m_{surf} (here $m_{\text{surf}} = 1.5$) and the scattering angle Ω , σ_s^2 is the slope variance, and f_{sh} accounts for the shadowing effect:

$$f_{\text{sh}}(k_y; \Omega) = \left[\frac{1 + \cos k_y(\pi - \Omega)}{2} \right]^3, \quad (8)$$

with k_y controlling the width of the shadowing function ($0 < k_y < 1$). The cosine of tilt angle of the facet surface normal for a particular illumination and view geometry is given by

$$\mu_n = \frac{\mu_v + \mu_0}{2} \left[\cos\left(\frac{\pi - \Omega}{2}\right) \right]^{-1}. \quad (9)$$

As the RPV model parameters, a_λ , k_λ and g_λ are wavelength dependent. As the microfacet model parameters, ε_λ is wavelength dependent and controls the weight of pBRDF while σ_s^2 and k_y are wavelength-independent angular shape parameters. Integration of the (1, 1) element of matrix \mathbf{R}_{surf} in equation (3) over $0 \leq \theta_v \leq \pi/2$ and $0 \leq (\phi_v - \phi_0) \leq 2\pi$ gives the directional-hemispheric reflectance (black sky albedo).

3.3. Polarized RT Modeling and Jacobian Evaluation

A hybrid RT model (MarCh-AD) is adopted here for modeling RT in the CASS (cf. Figure 2). The concept is the same as that proposed for a coupled atmosphere-ocean system [Xu *et al.*, 2016] with the exception that the ocean system is replaced by a land surface modeled as described in the previous section. The Markov chain method [Esposito and House, 1978; Esposito, 1979; Xu *et al.*, 2010, 2011, 2012] is used for polarized RT modeling in the vertically inhomogeneous aerosol/Rayleigh mixed layer, and the doubling method [Stokes, 1862; van de Hulst, 1963; Hansen, 1971; de Haan *et al.*, 1987; Evans and Stephens, 1991, among others] is used for modeling polarized RT in the Rayleigh scattering layer. The radiative fields from different layers are coupled using an adding strategy to obtain the top-of-atmosphere (TOA) fields [Xu *et al.*, 2016].

The advantages of this multilayer CASS model is twofold. First, it combines the strengths of Markov chain and doubling methods for efficiently modeling vertically inhomogeneous and homogeneous media, respectively. Second, it provides an efficient Jacobian calculation and optimization-based retrieval by saving the local RT field for different layers from forward modeling and then reusing them for Jacobian evaluation as long as they remain unchanged after a given aerosol or surface parameter is perturbed, and only the RT in the corresponding layer needs reevaluation. Since optimization-based retrievals involve Jacobian evaluations for a large number of parameters at all iterative steps, this strategy significantly improves the optimization efficiency.

It should be noted that the multilayer CASS model depicted in Figure 2 assumes the sensor to be above the top of atmosphere and the column to be free of trace-gas contamination. In the practical realization, however, the radiative field is evaluated at the sensor location (within the atmosphere for an airborne instrument) and gas absorption is corrected [Xu *et al.*, 2016]. Moreover, we assume single aerosol species representation of an effective set of aerosol optical properties, size distribution, and vertical profile. As parameterized in Table 1, a finite set of lognormal size distribution components ($N_{\text{sc}} = 5$) is used to represent the aerosol size, with median radii and standard deviations. And size-independent refractive index is assumed. Retrieval with more size components has also been performed, and comparison shows that they both represent well overall aerosol optical properties as long as these components are optimally chosen [Dubovik *et al.*, 2006]. Nevertheless, our retrieval is open for adopting more size components and/or more aerosol species with size-dependent refractive index depending on the availability of extra constraints and sensitivities from models or observations.

4. Retrieval Methodology and Uncertainty Estimate

4.1. Multipatch Algorithm for Coupled Aerosol Property and Surface Reflection Retrieval

The performance of an optimization approach depends on the construction and control of various types of physical or modeling constraints as well as proper use of a priori estimates. The fundamental idea of the

multipatch algorithm is the imposition of constraints to smooth (a) horizontal variations of aerosol loadings, microphysical properties including size distribution, refractive index, nonspherical particle fraction; (b) temporal variation of surface reflection properties; and (c) spectral variations of aerosol refractive indices and a set of spectral parameters for the surface BRDF and pBRDF. Imposition of all these constraints leads to the following cost function describing the difference between the model and a temporal series of images consisting of a total of N pixels [Dubovik et al., 2011],

$$\begin{aligned}
 \mathbf{C}(\mathbf{x}) &= \sum_{i=1}^N \Psi(\mathbf{x}_i) + \frac{1}{2} \mathbf{x}^T \Omega_{\text{interpatch}} \mathbf{x} \\
 &= \sum_{i=1}^N [\Psi_f(\mathbf{x}_i) + \Psi_s(\mathbf{x}_i) + \Psi_a(\mathbf{x}_i)] + \frac{1}{2} \mathbf{x}^T \Omega_{\text{interpatch}} \mathbf{x} \\
 &= \frac{1}{2} \sum_{i=1}^N \left[\Delta \mathbf{y}_i^T \mathbf{W}_{f,i}^{-1} \Delta \mathbf{y}_i + \gamma_s \mathbf{x}_i^T \Omega_{s,i} \mathbf{x}_i + \gamma_a (\mathbf{x}_i - \mathbf{x}_i^*)^T \mathbf{W}_{a,i}^{-1} (\mathbf{x}_i - \mathbf{x}_i^*) \right] + \frac{1}{2} \mathbf{x}^T \Omega_{\text{interpatch}} \mathbf{x},
 \end{aligned} \tag{10}$$

where \mathbf{x}_i is an iterative solution for a set of parameters being retrieved and \mathbf{x}_i^* is an a priori estimate of the solution corresponding to the i th patch, $\mathbf{x} = [\mathbf{x}_1, \mathbf{x}_2, \mathbf{x}_3, \dots, \mathbf{x}_N]$; $\Psi_f(\mathbf{x}_i)$, $\Psi_s(\mathbf{x}_i)$, and $\Psi_a(\mathbf{x}_i)$ correspond to the residues of fitting observations, the spectral smoothness constraints, and the a priori estimate, respectively; $\Omega_{s,i}$ is a smoothness matrix for constraining the spectral variation of a few aerosol microphysical properties and surface reflection properties across neighboring spectral wavelengths; \mathbf{W}_f and \mathbf{W}_a are the weighting matrices for measurements and the a priori estimate, respectively; γ denotes the relevant Lagrange multipliers that control the strength of the constraints; $\Delta \mathbf{y}_i$ is the difference between the model and measurements for the i th patch [$\Delta \mathbf{y}_i = \mathbf{y}(\mathbf{x}_i) - \mathbf{y}_{\text{meas}}$]; and $\Omega_{\text{interpatch}}$ is the interpatch smoothness matrix constructed for certain microphysical and horizontal distribution properties above patches along two orthogonal directions (u and v) of the image and for surface reflection parameters along temporal direction (t), namely

$$\Omega_{\text{interpatch}} = \gamma_u \mathbf{S}^{(m_u),T} \mathbf{S}^{(m_u)} + \gamma_v \mathbf{S}^{(m_v),T} \mathbf{S}^{(m_v)} + \gamma_t \mathbf{S}^{(m_t),T} \mathbf{S}^{(m_t)}, \tag{11}$$

where the derivative matrix $\mathbf{S}^{(m)}$ is constructed from m th order differences. The values of the multipliers (γ_u, γ_v) and γ_t used in our retrieval are shown in Table 2. They are dynamically updated during optimization iteration process [Dubovik, 2004; Xu et al., 2016].

The optimal solution is approached in an iterative way so that after k iterations, the solution vector $\mathbf{x}_{i,k+1}$ containing parameters of all aerosol and surface parameters for i th patch is updated as

$$\mathbf{x}_{i,k+1} = \mathbf{x}_{i,k} - t_p \Delta \mathbf{x}_{i,k}, \tag{12}$$

where the multiplier t_p ($0 \leq t_p \leq 1$) is introduced to improve the convergence of the nonlinear numerical algorithm [Ortega and Reinboldt, 1970].

Solving the following equation at the k th iteration gives an update of the solution vector $\Delta \mathbf{x}$,

$$\mathbf{A} \times (\Delta \mathbf{x})^T = [\nabla \Psi(\mathbf{x}) + \Omega_{\text{interpatch}} \mathbf{x}^T], \tag{13}$$

where the overall Fischer matrix is

$$\mathbf{A} = \begin{pmatrix} \mathbf{A}_{1,k} & 0 & \cdots & 0 \\ 0 & \mathbf{A}_{2,k} & \cdots & 0 \\ \cdots & \cdots & \cdots & \cdots \\ 0 & 0 & \cdots & \mathbf{A}_{N,k} \end{pmatrix} + \Omega_{\text{interpatch}} \tag{14}$$

Table 2. Parameters in Coupled Aerosol Property and Land Surface Reflection Retrieval, Their Initial Guess, and Order of Difference and Lagrange Multipliers for Imposing Smoothness Constraints

	Range	Initial Guess	Order of Finite Difference for Spectral Smoothness Constraints (m_s)	Lagrange Regularization Factor (γ_s)	Order of Finite Difference for Spatial Smoothness Constraints ($m_{(u,v)}$)	Lagrange Regularization Factor ($\gamma_{(u,v)}$)	Order of Finite Difference for Temporal Smoothness Constraints (m_t)	Lagrange Regularization Factor (γ_t)
<i>Aerosol Parameters</i>								
Volume concentration of size components ($C_{v,k}$, $\mu\text{m}^3/\mu\text{m}^2$)	$[1.0 \times 10^{-6}, 5]$	0.002	-	-	1	1	-	-
Mean height of aerosol distribution profile (h_a , km)	[0.05, 10]	1	-	-	1	0.01	-	-
Width of aerosol distribution profile (σ_a)	[0.5, 2.5]	0.75	-	-	1	0.01	-	-
Refractive index (real part: $n_r(\lambda)$)	[1.33, 1.60]	1.50	1	0.1	1	10	-	-
Refractive index (imaginary part: $n_i(\lambda)$)	$[5.0 \times 10^{-7}, 5.0 \times 10^{-1}]$	0.005	2	0.01	1	1	-	-
Nonspherical particle fraction (f_{ns})	[0, 0.5]	0.05	-	-	1	0.1	-	-
<i>Surface Parameters</i>								
BRDF spectral weight (a_j)	[0, 0.7]	0.015–0.1	3	0.1	-	-	1	0.5
Anisotropy parameter k_λ	[0, 1]	0.6	1	0.5	-	-	1	0.5
Anisotropy parameter g_λ	[-1, 1]	0.1	1	0.5	-	-	1	0.5
pBRDF weight ε_λ	[0, 10]	0.01	1	0.5	-	-	1	0.5
Shadowing width k_γ	[0, 1]	0.75	-	-	-	-	1	0.5
Slope variance σ_s^2	[0.05, 0.5]	0.015	-	-	-	-	1	0.5

with the component for the i th patch expressed as a function of Jacobian matrix $\mathbf{J}_{i,k}$ and weighting matrix $\mathbf{W}_{f,ji}$

$$\mathbf{A}_{1,k} = \mathbf{J}_{i,k}^T \mathbf{W}_{f,i}^{-1} \mathbf{J}_{i,k} + \gamma_{\Delta,i} \Omega_{\Delta,i} + \gamma_{a,i} \mathbf{W}_{a,i}^{-1} \quad (15)$$

and

$$\nabla \Psi(\mathbf{x}) = [\nabla \Psi(\mathbf{x}_{1,k}) \quad \nabla \Psi(\mathbf{x}_{2,k}) \quad \dots \quad \nabla \Psi(\mathbf{x}_{N,k})], \quad (16)$$

with $\nabla \Psi(\mathbf{a}_{i,k})$ being the gradient of the minimized quadratic form:

$$\nabla \Psi(\mathbf{x}_{i,k}) = \mathbf{J}_{i,k}^T \mathbf{W}_{f,i}^{-1} (\mathbf{y}_{i,k} - \mathbf{y}_{i,\text{obs}}) + \gamma_{s,i} \Omega_{s,i} \mathbf{x}_{i,k} + \gamma_{a,i} \mathbf{W}_{a,i}^{-1} (\mathbf{x}_{i,k} - \mathbf{x}_i^*). \quad (17)$$

In the above equations, \mathbf{y}_{obs} contains the measurement/observation data; \mathbf{y}_k contains the modeled radiance and polarization with \mathbf{x}_k ; \mathbf{W}_f is the weighting matrix defined as the covariance matrix \mathbf{C}_f normalized by its first diagonal element, $\mathbf{W}_f = \mathbf{C}_f / C_{f,1}$; \mathbf{W}_a is the weighting matrix of the a priori estimate \mathbf{x}^* ; and Ω_s is the single patch-based smoothness matrix containing subsmoothness matrices for all parameters.

Taking into account both aerosol and surface parameters (see Table 2), the solution vector \mathbf{x} consists of log $[m_{r,j}, m_{i,j}, C_{v,k}, h_a, \sigma_a, f_{ns}, a_{\lambda,j}, k_{\lambda,j}, g_{\lambda,j}, \varepsilon_{\lambda,j}, k_\gamma, \sigma_s^2]^T$, $j = 1, \dots, N_{\lambda}$ and $k = 1, \dots, N_{sc}$, where N_{λ} is the total number of wavelength used in retrieval (e.g., $N_{\lambda} = 7$ for AirMSPI aerosol/surface retrieval) and N_{sc} is the total number of aerosol size components (e.g., $N_{sc} = 5$ in the current study), and the natural logarithm is used to ensure nonnegativity of the true solution after dynamic updates during the iterative optimization process. Then $\gamma_s \Omega_s$ is constructed as a block matrix from diagonal concatenation of the spectral smoothness matrices for real and imaginary parts of refractive index and Δa_{λ} , namely for all patches,

$$\gamma_s \Omega_s = \text{diag} \left\{ \gamma_{s,m_r}, \Omega_{s,m_r}, \gamma_{s,m_i}, \Omega_{s,m_i}, \mathbf{0}, \mathbf{0}, \mathbf{0}, \mathbf{0}, \gamma_{s,a}, \Omega_{s,a}, \gamma_{s,k}, \Omega_{s,k}, \gamma_{s,g}, \Omega_{s,g}, \gamma_{s,\varepsilon}, \Omega_{s,\varepsilon}, \mathbf{0}, \mathbf{0} \right\}, \quad (18)$$

where $\mathbf{0}$ represents a zero submatrix for a parameter without being subject to any smoothness constraints; and the Lagrange multipliers γ_s are predetermined using the methodology of Dubovik [2004] and are given in Table 2.

In our retrieval tests, an a priori estimate of the solution is assumed unavailable so we set $\mathbf{x}_{i,k} = \mathbf{x}_i^*$. On such a basis, equation (17) simplifies to

$$\nabla\Psi(\mathbf{x}_{i,k}) = \mathbf{J}_{i,k}^T \mathbf{W}_{f,j}^{-1} (\mathbf{y}_{i,k} - \mathbf{y}_{i,\text{obs}}) + \gamma_{s,i} \Omega_{s,i} \mathbf{x}_{i,k}. \quad (19)$$

The retrieval is deemed successful when the minimization of the cost function is achieved, such that

$$2 \sum_{i=1}^{N_{\text{patch}}} \Psi(\mathbf{x}_{k,i}) + \mathbf{x}_k \Omega_{\text{interpatch}} \mathbf{x}_k^T \leq N_{\text{interpatch}} \varepsilon_f^2 + \sum_{i=1}^{N_{\text{patch}}} (N_{f,i} + N_{s,i} + N_{x^*,i} - N_{x,i}) \varepsilon_f^2, \quad (20)$$

where $N_{f,i}$, $N_{s,i}$, $N_{x,i}$ and $N_{x^*,i}$ are the number of observations, spectral smoothness, unknowns, and a priori estimates of parameters corresponding to the i th patch, respectively; $N_{\text{interpatch}}$ is the number of spatial smoothness constraints; and ε_f^2 is the expected variance due to measurement errors. In practice, equation (20) is not often satisfied due to the presence of forward RT modeling errors and other unmodeled effects. Therefore, as the second criterion, the retrieval is terminated when the relative difference of fitting residues with solutions from two successive iterations drops below a user-specified threshold value, ε_c^2 .

4.2. Retrieval Error Estimate

Both instrumental errors and physical constraints imposed on the retrievals must be taken into account when evaluating retrieval errors. In terms of instrumental errors, we consider two types of errors, random ($\Delta\mathbf{y}_{\text{rand}}^{\text{obs}}$) and systematic errors ($\Delta\mathbf{y}_{\text{syst}}$). The latter include absolute error ($\Delta\mathbf{y}_{\text{abs}}^{\text{obs}}$), band-to-band error ($\Delta\mathbf{y}_{\text{b2b}}^{\text{obs}}$), and camera-to-camera error ($\Delta\mathbf{y}_{\text{c2c}}^{\text{obs}}$) which appears when multiple cameras are used to make multiangular observation (as with MISR), and forward modeling error ($\Delta\mathbf{y}^{\text{model}}$) results from the use of a 1-D RT model.

We start with error analysis for a single-patch retrieval before generalizing it to the multipatch case. By considering a priori smoothness constraints constructed for wavelength-dependent aerosol refractive index and surface reflection parameters, an a priori estimate of the solution, and propagation of instrumental random and systematic errors, the overall covariance matrix for error estimate for single-patch optimization is expressed as

$$\mathbf{C}_{\Delta\mathbf{x},\text{syst}} = \Delta\mathbf{x}_{\text{syst}} (\Delta\mathbf{x}_{\text{syst}})^T + \mathbf{C}_{\Delta\mathbf{x},\text{rand}}, \quad (21)$$

where

$$\Delta\mathbf{x}_{\text{syst}} = \mathbf{A}^{-1} \nabla\Psi, \quad (22)$$

$$\mathbf{C}_{\Delta\mathbf{x},\text{rand}} = \mathbf{A}^{-1} \varepsilon_{\text{rand}}^2 \quad (23)$$

where $\varepsilon_{\text{rand}}$ is the random noise, \mathbf{A} is computed at the retrieved solution \mathbf{x} via equation (15), and $\nabla\Psi$ is given by

$$\nabla\Psi = \mathbf{J}^T \mathbf{W}_f^{-1} \Delta\mathbf{y}_{\text{syst}} + \gamma_s \Omega_s \mathbf{x}^{\text{true}} + \gamma_a \mathbf{W}_a^{-1} (\mathbf{x}^{\text{true}} - \mathbf{x}^*), \quad (24)$$

where the total systematic error is expressed as

$$(\Delta\mathbf{y}_{\text{syst}})^2 = (\Delta\mathbf{y}_{\text{abs}}^{\text{obs}})^2 + (\Delta\mathbf{y}_{\text{b2b}}^{\text{obs}})^2 + (\Delta\mathbf{y}_{\text{c2c}}^{\text{obs}})^2 + (\Delta\mathbf{y}^{\text{model}})^2 \quad (25)$$

from assuming no intercorrelations. Note that all Lagrange factors involved in the Jacobian matrix and $\nabla\Psi$ evaluations are equal to their updated values associated with the last iteration. To estimate errors for functions of the retrieved parameters (namely $y = f(\mathbf{x})$, e.g., SSA), the chain rule is applied so that in the matrix form

$$\Delta y = \sqrt{\mathbf{J}_y^T \mathbf{C}_{\Delta \mathbf{x}} \mathbf{J}_y}, \quad (26)$$

where \mathbf{J}_y denotes the Jacobian array containing derivatives of y with respect to all retrieved parameters x that are relevant to the calculation of y .

For multipatch optimization, we further account for a priori smoothness constraints imposed on aerosol and surface variations across spatially and temporally neighboring patches so that the retrieval error for a multipatch system due to systematic errors is

$$\Delta \mathbf{x}_{\text{syst}} = \left[\begin{pmatrix} \mathbf{A}_1 & \mathbf{0} & \dots & \mathbf{0} \\ \mathbf{0} & \mathbf{A}_2 & \dots & \mathbf{0} \\ \dots & \dots & \dots & \dots \\ \mathbf{0} & \mathbf{0} & \dots & \mathbf{A}_N \end{pmatrix} + \mathbf{\Omega}_{\text{interpatch}} \right]^{-1} \left[\begin{pmatrix} \nabla\Psi_1 \\ \nabla\Psi_2 \\ \dots \\ \nabla\Psi_N \end{pmatrix} + \mathbf{\Omega}_{\text{interpatch}} \mathbf{x}^{\text{true}} \right], \quad (27)$$

which result from systematic errors in the measurements and from forward modeling:

$$(\Delta \mathbf{y}_{i,\text{syst}})^2 = (\Delta \mathbf{y}_{i,\text{p2p}}^{\text{obs}})^2 + (\Delta \mathbf{y}_{i,\text{abs}}^{\text{obs}})^2 + (\Delta \mathbf{y}_{i,\text{b2b}}^{\text{obs}})^2 + (\Delta \mathbf{y}_{i,\text{c2c}}^{\text{obs}})^2 + (\Delta \mathbf{y}_i^{\text{model}})^2, \quad (28)$$

where we further account for the systematic component of pixel-to-pixel error ($\Delta \mathbf{y}_{i,\text{p2p}}^{\text{obs}}$) in addition to the three types of single-pixel-related systematic errors. The first four terms on the right-hand side of the above two subequations form the systematic errors contributed by observation uncertainties, and the last term indicates the contribution of modeling error.

As the second source of error, random noise propagates to the retrieval via the following covariance matrix

$$\mathbf{C}_{\Delta \mathbf{x}, \text{rand}} = \left[\begin{pmatrix} \mathbf{A}_1 & \mathbf{0} & \dots & \mathbf{0} \\ \mathbf{0} & \mathbf{A}_2 & \dots & \mathbf{0} \\ \dots & \dots & \dots & \dots \\ \mathbf{0} & \mathbf{0} & \dots & \mathbf{A}_N \end{pmatrix} + \mathbf{\Omega}_{\text{interpatch}} \right]^{-1} \varepsilon_{\text{rand}}^2. \quad (29)$$

Summing over the contribution by both systematic and random errors, the overall error is estimated by taking the diagonal term of the retrieval error covariance matrix, namely

$$\Delta x_j = \sqrt{(\mathbf{C}_{\Delta \mathbf{x}})_{jj}}, \quad (30)$$

and

$$\mathbf{C}_{\Delta \mathbf{x}} = \Delta \mathbf{x}_{\text{syst}} (\Delta \mathbf{x}_{\text{syst}})^T + \mathbf{C}_{\Delta \mathbf{x}, \text{rand}}. \quad (31)$$

By performing the above error analysis, it is assumed that the modeling error and the four types of systematic errors of an instrument in equation (28) are well characterized. Indeed, their quantification is rather difficult due to the complexity of error analysis for a sensor that consists of multiple optical units as well as the under-characterization of multiple sources of modeling errors such as imperfections in the surface reflection model, cloud contamination, etc., which can bias the spectral and angular remote sensing signals.

For practicality, the square root of the diagonal terms of the following covariance matrix is used for the error estimate

$$\mathbf{C}_{\Delta\mathbf{x}} = \Delta\mathbf{x}_{\text{sys}}(\Delta\mathbf{x}_{\text{sys}})^T + \mathbf{C}_{\Delta\mathbf{x}, \text{rand}}, \quad (32)$$

with $\mathbf{C}_{\Delta\mathbf{x}, \text{rand}}$ expressed by equation (29) and $\Delta\mathbf{x}_{\text{sys}}$ expressed by

$$\Delta\mathbf{x}_{\text{sys}} = \left[\begin{pmatrix} \mathbf{A}_1 & \mathbf{0} & \dots & \mathbf{0} \\ \mathbf{0} & \mathbf{A}_2 & \dots & \mathbf{0} \\ \dots & \dots & \dots & \dots \\ \mathbf{0} & \mathbf{0} & \dots & \mathbf{A}_N \end{pmatrix} + \mathbf{\Omega}_{\text{interpatch}} \right]^{-1} \left[\begin{pmatrix} \nabla\Psi_1 \\ \nabla\Psi_2 \\ \dots \\ \nabla\Psi_N \end{pmatrix} + \mathbf{\Omega}_{\text{interpatch}}\mathbf{x}^{\text{true}} \right], \quad (33)$$

where

$$\nabla\Psi_i = \mathbf{J}_i^T \mathbf{W}_{f,i}^{-1} [\mathbf{y}_i(\mathbf{x}_i^{\text{retrieved}}) - \Delta\mathbf{y}_{i,\text{obs}}] + \gamma_{s,i} \mathbf{\Omega}_{s,i} \mathbf{x}_i^{\text{retrieved}} + \gamma_{a,i} \mathbf{W}_{a,i}^{-1} (\mathbf{x}_i^{\text{retrieved}} - \mathbf{x}_i^*). \quad (34)$$

It can be observed from the above equation that, as the retrieved solution is the closest estimate of the “true” solution \mathbf{x}^{true} , we assume $\mathbf{x}^{\text{true}} = \mathbf{x}^{\text{retrieved}}$. When a priori \mathbf{x}^* is not available, we assume $\mathbf{x}^* = \mathbf{x}^{\text{true}}$, which means the last term on the right-hand side of above equation disappears (namely $\gamma_{a,i} \mathbf{W}_{a,i}^{-1} (\mathbf{x}_i^{\text{true}} - \mathbf{x}_i^*) = 0$). Moreover, in the absence of observation errors, $\Delta\mathbf{x}_{\text{sys}}$ obtained from equation (33) denotes the bias caused by modeling errors. In the presence of observation errors, equation (29) is included to treat observation errors as random. Indeed, instrument errors are already contained in the observation \mathbf{y}_{obs} . Therefore, by implementing equations (29), (32), and (33), it is possible that errors are double counted in the case that they bias the solution in the same direction as the modeling errors, resulting in a conservative error estimate.

Most error estimates involving Jacobians assume that the calculation is representative of the whole solution space and that the retrieval error is linear with measurement error. These two assumptions can be problematic in situations where model and/or observation errors are large. In these cases, closure tests using synthetic data with combined random and systematic errors to obtain improved error estimates are recommended [Dubovik et al., 2011; Xu et al., 2016].

5. Retrieval Application to AirMSPI Data

The retrieval algorithm is oriented for retrieving column aerosol and surface reflection properties from observations by AirMSPI, which operates in eight spectral channels: 355, 380, 445, 470*, 555, 660*, 865*, and 935 nm, with the asterisk denoting polarimetric bands in which the Stokes parameters Q and U are measured in addition to radiance I . Images of a targeted area were obtained at nine viewing angles: 0° (nadir), $\pm 29^\circ$, $\pm 48^\circ$, $\pm 59^\circ$, and $\pm 66^\circ$. At nadir, the imaged area covers a 10 km \times 11 km region and the data are mapped to a 10 m spatial grid. We aggregate 50 by 50 pixels into a “patch” to mitigate the errors from independent pixel/patch approximation in RT theory and to reduce computational costs. Without using the water vapor influenced band (935 nm), a total of 117 signals per patch are used, which include 63 radiances at 9 angles and 7 spectral bands, and 27 signals of $q = Q/I$ and another 27 signals of $u = U/I$ in the 3 polarimetric bands. Retrieval for all patches of a surface area viewed from all nine angles is performed at one time.

5.1. AirMSPI Data Sets

A wide range of atmospheric conditions and terrestrial environments have been covered by AirMSPI during more than a hundred flights from several airborne campaigns. These include PODEX (January to February 2013), SEAC⁴RS (August to September 2013), CalWater-2 (January to March 2015), ImPACT-PM (July 2016), and ObserVations of Aerosols above CLouds and their intERactionS (ORACLES, August to September 2016). The latter is not included in this paper since most data acquisitions occurred over ocean for which a

Table 3. Information of Collocated AERONET Sites Involved in Retrieval Validation (Level 1.5 Products Are Used)

Case #	Campaign	Collocated AERONET Site	Lon (°W), Lat (°N)	Date (UTC)	Solar Zenith Angle (deg)	AOD AERONET, 500 nm	Collated AERONET Time (UTC)	Collated AirMSPI Time (UTC)
1	PODEX	Hanford	119.643, 36.316	20130118	65.5	0.13	17:39	17:50
2	PODEX	Bakersfield	119.000, 35.332	20130122	56.1	0.24	19:10	19:17
3	PODEX	Fresno	119.773, 36.785	20130131	58.9	0.10	18:30	18:34
4	PODEX	Porterville	119.055, 36.032	20130131	56.9	0.13	18:13:19:13	18:44
5	PODEX	Huron	120.105, 36.206	20130131	55.7	0.10	19:16	19:07
6	PODEX	Fresno	119.773, 36.785	20130131	54.4	0.12	20:26:21:15	20:41
7	PODEX	Porterville	119.055, 36.032	20130131	54.0	0.11	21:13	20:50
8	PODEX	Bakersfield	119.000, 35.332	20130131	56.8	0.14	21:09:22:13	21:40
9	PODEX	Hanford	119.643, 36.316	20130131	58.4	0.13	21:57	21:51
10	SEAC ⁴ RS	Arkansas	93.203, 35.826	20130906	68.5	0.13	22:59	22:42
11	SEAC ⁴ RS	Baskin	91.739, 32.282	20130909	58.1	0.27	21:36:21:58	21:45
12	SEAC ⁴ RS	Baskin	91.739, 32.282	20130909	62.5	0.27	21:58	22:03
13	SEAC ⁴ RS	RailroadValley	115.962, 38.504	20130923	52.8	0.30	21:38:22:38	22:12
14	P-E ^a	Fresno	119.773, 36.782	20120106	59.4	0.51	20:08	20:23
15	CalWater	Monterey ^b	121.855, 36.593	20150131	56.1	0.03	21:23	21:26
16	CalWater	Fresno	119.773, 36.785	20150131	58.1	0.33	21:21	21:42
17	CalWater	Fresno	119.773, 36.785	20150217	51.0	0.17	19:16	19:08
18	ImPACT-PM	Fresno	119.773, 36.785	20160705	25.3	0.08	18:05	18:26
19	ImPACT-PM	Fresno	119.773, 36.785	20160705	14.1	0.09	19:05	20:06
20	ImPACT-PM	Fresno	119.773, 36.785	20160705	16.5	0.08	19:05:22:05	20:43
21	ImPACT-PM	Bakersfield	119.000, 35.332	20160705	13.8	0.10	19:31:19:46	19:37
22	ImPACT-PM	Bakersfield	119.000, 35.332	20160705	21.0	0.08	21:16	21:17
23	ImPACT-PM	Bakersfield	119.000, 35.332	20160707	14.0	0.10	19:31	19:32
24	ImPACT-PM	Fresno	119.773, 36.785	20160705	14.9	0.09	20:19:20:34	20:25
25	ImPACT-PM	Fresno	119.773, 36.785	20160705	18.6	0.07	20:34:21:49	21:00
26	ImPACT-PM	Fresno	119.773, 36.785	20160707	21.1	0.06	19:06	18:52
27	ImPACT-PM	Bakersfield	119.000, 35.332	20160708	20.9	0.08	18:46	18:45

^aData were from AirMSPI preengineering (P-E) flight.

^bOnly land part of the image with coexistence of ocean and land was used.

version of our aerosol retrieval algorithm has been developed [Xu *et al.*, 2016]. The various field campaigns had different purposes, including exploration of the impact of aerosols on clouds and precipitation (CalWater-2), meteorology and climate (SEAC⁴RS), air quality (SEAC⁴RS and ImPACT-PM), and comparison of different polarimetric sensing approaches for aerosol and cloud characterization (PODEX). This paper also includes an additional data set from an AirMSPI preengineering flight on 6 January 2012, during which a moderately high AOD (~ 0.45 at 0.55 μm) was observed over Fresno, California. From these campaigns/flights, 27 AirMSPI step-and-stare data collection sequences were identified to be cloud free and collocated with Aerosol Robotic Network (AERONET) land sites for retrieval validation. Locations of these AERONET sites and AirMSPI/AERONET measurement times are listed in Table 3.

5.2. Retrieval Validation Against AERONET Products

The retrieved AirMSPI AOD, SSA, size distribution, and refractive index are validated against AERONET Level 1.5 aerosol products. As a first check, a retrieval is performed using AirMSPI observations acquired over the AERONET Fresno site on 6 January 2012. The left and middle subimages of Figure 3a show the radiance images using different spectral band combinations. The right subimage displays degree of linear polarization (DOLP) in the three polarimetric bands. Figure 3b shows images of bidirectional reflectance factor (BRF) at blue (445 nm), green (555 nm), and red (660 nm) bands in the left, middle, and right panels, respectively, for the retrieval area with spatial resolution ~0.5 km (i.e., the corrected patch size). BRF is defined as $\pi I_{\text{meas}} d^2 / \mu_0 E_0$, where I_{meas} is the measured radiance, d is the Earth-Sun distance, μ_0 is the cosine of solar zenith angle, and E_0 is the exo-atmospheric solar irradiance. Figure 3c shows the maps of retrieved AOD, SSA, and surface albedo (A) at 555 nm in the left, middle, and right panels, respectively. The retrieved AOD, SSA, and volume-weighted aerosol size distribution for the atmosphere above the patch closest to

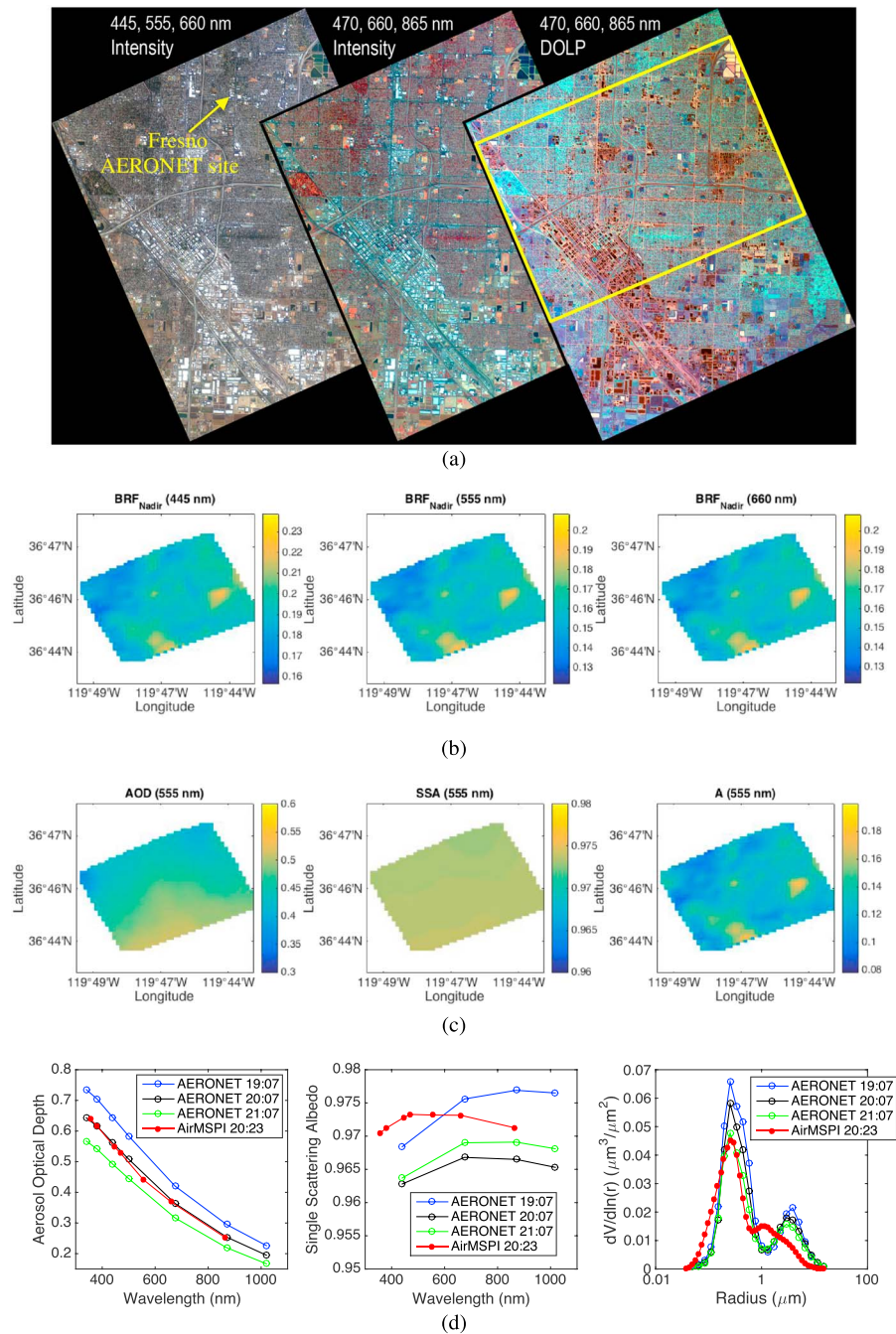


Figure 3. (a) High-resolution (10 m) AirMSPI nadir imagery of Fresno, CA, acquired on 6 January 2012 [Diner et al., 2013]. The left and middle images are radiance data using different spectral band combinations. The location of the Fresno AERONET site is marked in the left image. The right image displays DOLP in the three polarimetric bands, and the yellow box indicates the area viewed at all nine AirMSPI view angles and where data are collected for retrieval. (b) Lower resolution imagery (~0.5 km) of the retrieval area after pixel aggregation. The left, middle, and right panels give the images of bidirectional reflectance factor (BRF) at blue (445 nm), green (555 nm), and red (660 nm) bands, respectively. BRF is defined as $\pi I_{\text{meas}} d^2 / \mu_0 E_0$, where I_{meas} is the measured radiance, d is the Earth-Sun distance, μ_0 is the cosine of solar zenith angle, and E_0 is the exo-atmospheric solar irradiance. (c) Retrieved AOD, SSA, and surface albedo (A) maps at 555 nm in the left, middle, and right panels, respectively, with patch resolution 0.5 km. (d) AirMSPI retrieved AOD, SSA, and volume-weighted aerosol size distribution at the patch closest to the Fresno AERONET site, compared to the AERONET-derived values.

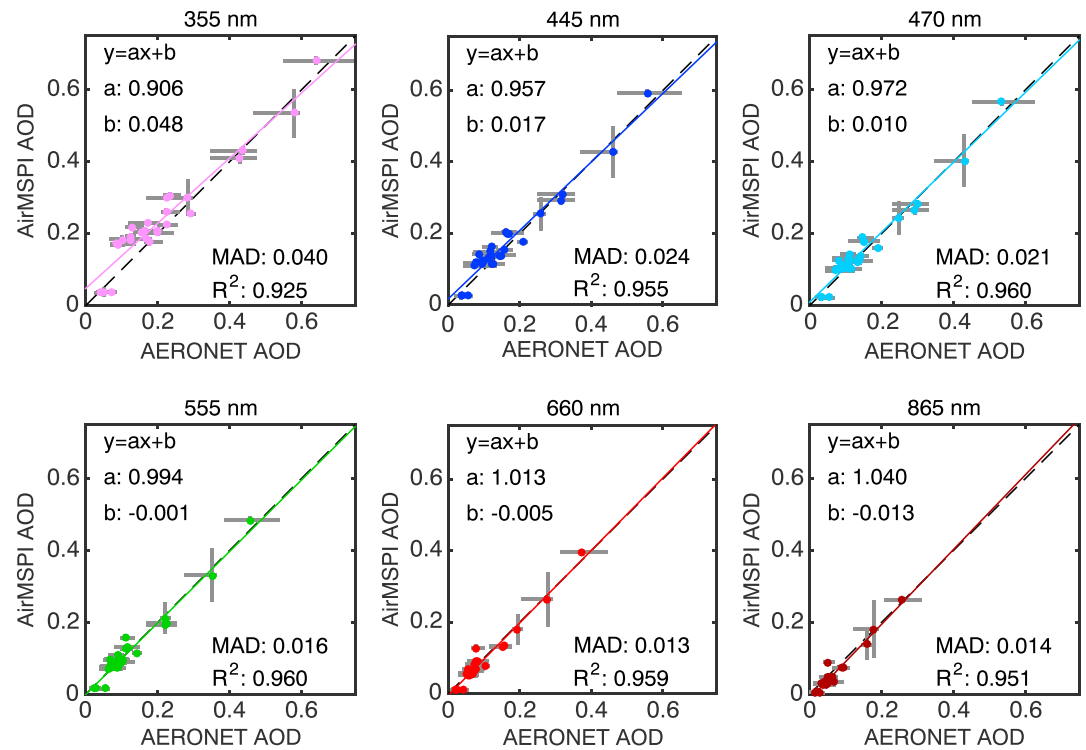


Figure 4. Regression of AirMSPI retrieved aerosol optical depth (AOD) against AERONET measured values: (top row) 355, 445, and 470 nm; (bottom row) 555, 660, and 865 nm. Linear interpolation is used to obtain AERONET AOD values at the AirMSPI wavelengths. The AERONET uncertainties are from the ± 1 h window around the time of AirMSPI overflight plus measurement uncertainties (0.01), while the AirMSPI uncertainties are the root-mean-square of the pixel-resolved errors over the whole image. Linear regression analysis yields values of slope “a,” intercept “b,” coefficient of determination “ R^2 ,” and mean absolute difference (MAD) as indicated in all panels.

the Fresno are compared to the AERONET reference data in the left, middle, and right panels of Figure 3d. Reasonably good agreement is obtained for all these quantities, except for the coarse particle size distribution, most likely due to the lack of shortwave infrared bands on AirMSPI.

To allow a direct validation, AERONET’s spectral aerosol products are linearly interpolated in wavelength to match up with AirMSPI band centers. To facilitate comparison of aerosol size, an effective radius is calculated for fine and coarse mode aerosols from

$$r_{\text{eff.fine/coarse}} = \left[\int_{r_1}^{r_2} \frac{dv(r)}{d \ln r} d \ln r \right] \left[\int_{r_1}^{r_2} \frac{1}{r} \frac{dv(r)}{d \ln r} d \ln r \right]^{-1}. \tag{35}$$

To be consistent with AERONET definition of fine and coarse mode aerosols, we set $r < r_{sp}$ and $r > r_{sp}$ for fine and coarse modes of aerosols, respectively, where the separation radius r_{sp} between the two modes is the minimum of volume concentration within the size interval [0.439, 0.992] μm (cf. AERONET Inversion Products (Version 2) document available at http://aeronet.gsfc.nasa.gov/new_web/Documents/Inversion_products_V2.pdf). Assuming water soluble aerosol sizes, the uncertainties associated with the AERONET retrieved volume concentrations of its 22 size components are estimated as 15–100% for $r < 0.1 \mu\text{m}$, 15% for $0.1 < r < 7 \mu\text{m}$, and $r > 7 \mu\text{m}$ [Dubovik et al., 2000]. The chain rule is used to calculate the uncertainties in effective radii of the fine and coarse mode size components.

Figures 4 and 5 compare AirMSPI and AERONET retrievals of AOD and SSA, whereas Figures 6 and 7 compare real and imaginary parts of aerosol refractive index. Comparisons of fine and coarse mode effective radii are

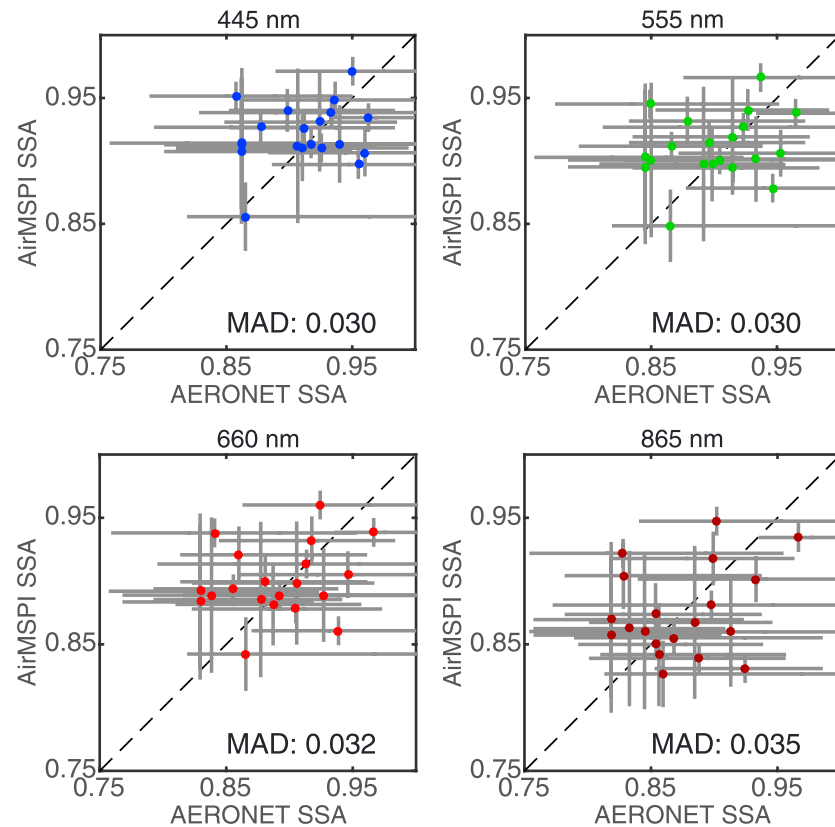


Figure 5. Regression of AirMSPI retrieved single-scattering albedo (SSA) against AERONET reference data: the SSA for (top left) 445 and (top right) 555 nm, and the SSA for (bottom left) 660 and (bottom right) 865 nm. Linear interpolation is used to obtain AERONET SSA values at the AirMSPI wavelengths. The AERONET retrieval uncertainties are adopted from *Dubovik et al.* [2000]. The AirMSPI errors are computed from statistics obtained over the whole image plus the errors evaluated using the method in section 4.2.

shown in Figure 8 together with uncertainties. The AERONET uncertainties consist of two parts: temporal variation within the ± 1 h window (if available) centered on the AirMSPI nadir overpass time over the target area and aerosol measurement/retrieval error [*Dubovik et al.*, 2000]. The AirMSPI uncertainties are estimated as the root-mean-square of the patch-resolved retrieval errors. For AOD and SSA, weighted linear regression is performed to obtain the slope a and intercept b as well as the coefficient of determination, R^2 . Values of these regression parameters as well as the mean absolute difference (MAD) are indicated in all panels. The AOD regression shows a spectrally mean R^2 of 0.95, mean slope $\bar{a} \approx 0.97$, and mean intercept $\bar{b} \approx 0.01$, which reflect high retrieval quality. While SSA and refractive index in Figures 5–7 show relatively larger differences between AirMSPI and AERONET retrievals, the differences are generally within their respective uncertainties which in turn depend on AirMSPI and AERONET observation errors and the sensitivities of observation to retrieval quantities. In addition, while Figure 8 (left panel) shows good agreement of AirMSPI and AERONET retrieved fine mode aerosol size (maximum $\sim 25\%$), relatively larger differences (maximum 65%) are observed in coarse mode aerosol size in Figure 8 (right panel). As noted above, shortwave infrared spectral bands, which AirMSPI lacks, are necessary to constrain the coarse mode aerosol size retrieval.

5.3. Benefits of Multiangular and Polarimetric Measurements

While the AirMSPI AOD and SSA retrievals demonstrate good agreement with AERONET reference data, these figures do not illustrate the relative value of multiangular and polarimetric observations in constraining the retrievals. To do this, a sensitivity study was performed using two, three, five, seven, and nine angles including radiance and polarization data from AirMSPI, and nine angles without polarimetric measurements (radiances

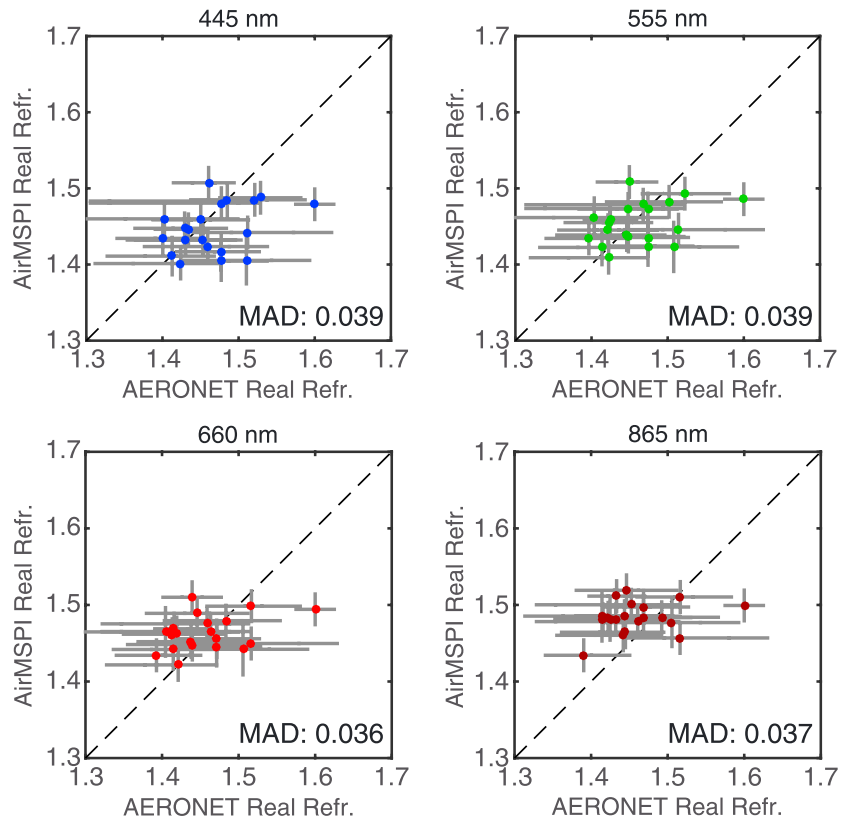


Figure 6. Same as Figure 5 but for the real part of the aerosol refractive index.

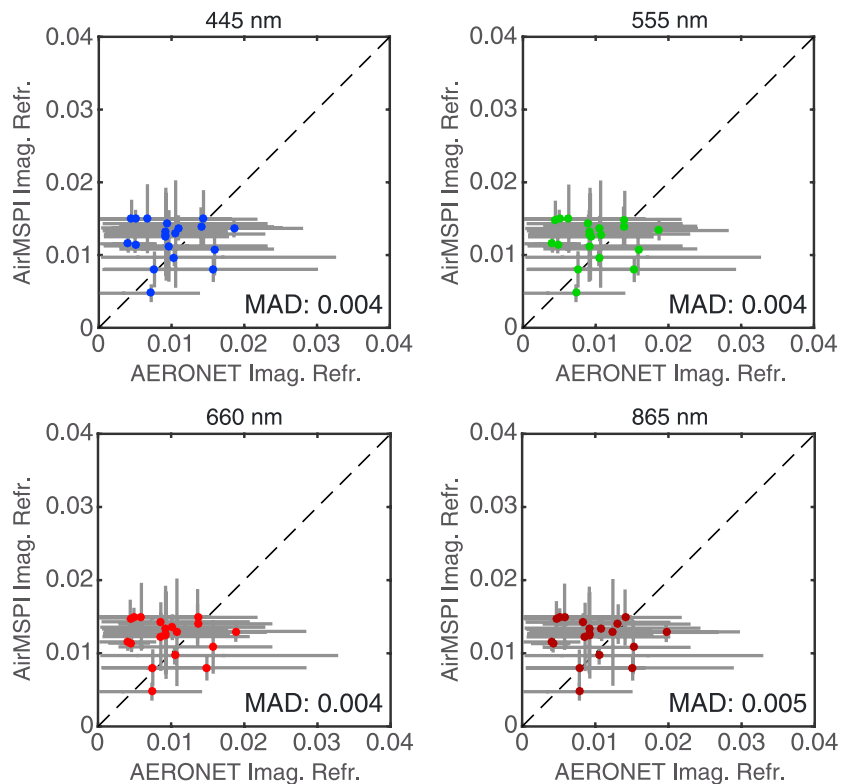


Figure 7. Same as Figure 5 but for the imaginary part of aerosol refractive index.

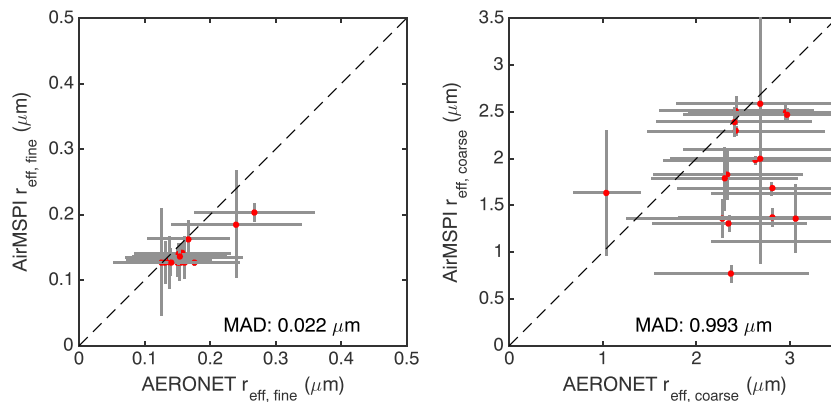


Figure 8. Same as Figure 5 but for the effective radii of fine and coarse mode aerosols.

in the 470, 660, and 865 nm band were retained). For the two-angle retrieval, individual retrievals were performed for all four pairs of symmetric angles about the nadir, namely $(-29^\circ, +29^\circ)$, $(-48^\circ, +48^\circ)$, $(-59^\circ, +59^\circ)$, and $(-66^\circ, +66^\circ)$. For N_{view} -angle retrieval ($N_{\text{view}} > 2$, N_{view} being odd), individual retrievals were performed for all combinations of $(N_{\text{view}}-1)/2$ pairs of symmetric angles plus nadir. For example, the five-angle retrieval involved individual runs of all six angular combinations $(0^\circ, \pm 29^\circ, \pm 48^\circ)$, $(0^\circ, \pm 29^\circ, \pm 59^\circ)$, $(0^\circ, \pm 29^\circ, \pm 66^\circ)$, $(0^\circ, \pm 48^\circ, \pm 59^\circ)$, $(0^\circ, \pm 48^\circ, \pm 66^\circ)$, and $(0^\circ, \pm 59^\circ, \pm 66^\circ)$. As demonstrated, Figures 9a and 9b give the AOD from two-angle and five-angle retrieval, respectively. The specific angular combination is given in the panel title. It can be observed that for both two-angle and five-angle retrieval, AOD retrieval accuracy has strong dependence on the specific angular combination. Measured from R^2 and the MAD of AOD, the angular set $[-66^\circ, 66^\circ]$ gives the best AOD for two-angle retrieval, while the angular set $[0, \pm 48^\circ, \pm 66^\circ]$ gives the best AOD for five-angle retrieval. Selecting the best angular combination from N_{view} -angle retrieval based on the R^2 and MAD metrics, Figure 10 (top row and bottom left and middle) shows a progressively improved AirMSPI-AERONET AOD regression quality with stronger correlation and reduced MAD when the number of view angles increases. The best angular set associated with the best retrieval is given in the panel title. These results clearly demonstrate that the most oblique view angles $[-66^\circ, 66^\circ]$ are the most valuable angles among all nine available AirMSPI views as they show up in all N_{view} -angle retrievals. The main reasons are that path radiance increases with view angle, thereby providing more information about aerosols, and oblique angles are less contaminated by surface reflection. It is possible that further improvement can be achieved by using even larger viewing angles ($\theta_{\text{view}} > 66^\circ$). However, this will limit the areal coverage overlap at all angles in step-and-stare mode and will degrade the spatial resolution for a gimbaled camera. Moreover, the plane-parallel atmosphere assumption with the forward radiative transfer model will be subject to increased modeling errors at larger viewing angles.

The results indicate that improved AOD retrieved from using more viewing angles “saturates” at around five-viewing angles as further increasing the number of viewing angles to 7 and 9 results in negligible benefit in terms of increasing R^2 and reducing MAD. The same effect is also observed from SSA retrieval in Figure 11, which indicated little gain of SSA retrieval accuracy with more than five angles. These results are basically consistent with the findings of Hasekamp and Landgraf [2007] using synthetic data analysis and of Wu *et al.* [2015] using RSP observations, who found that the retrieval performance is not significantly improved when more than five-viewing angles are used. This conclusion appears robust despite the differences in instrument characteristics between AirMSPI and RSP and differences in the retrieval algorithms.

Polarization signals contain strong sensitivity about aerosol microphysical properties including refractive index and size distribution that determine aerosol scattering and absorption properties. Polarimetry is expected to reduce retrieval errors that are observed from radiance-only retrievals. As a justification, we compare nine-angle retrieval with and without polarization in Figures 10 (bottom middle and right) and 11

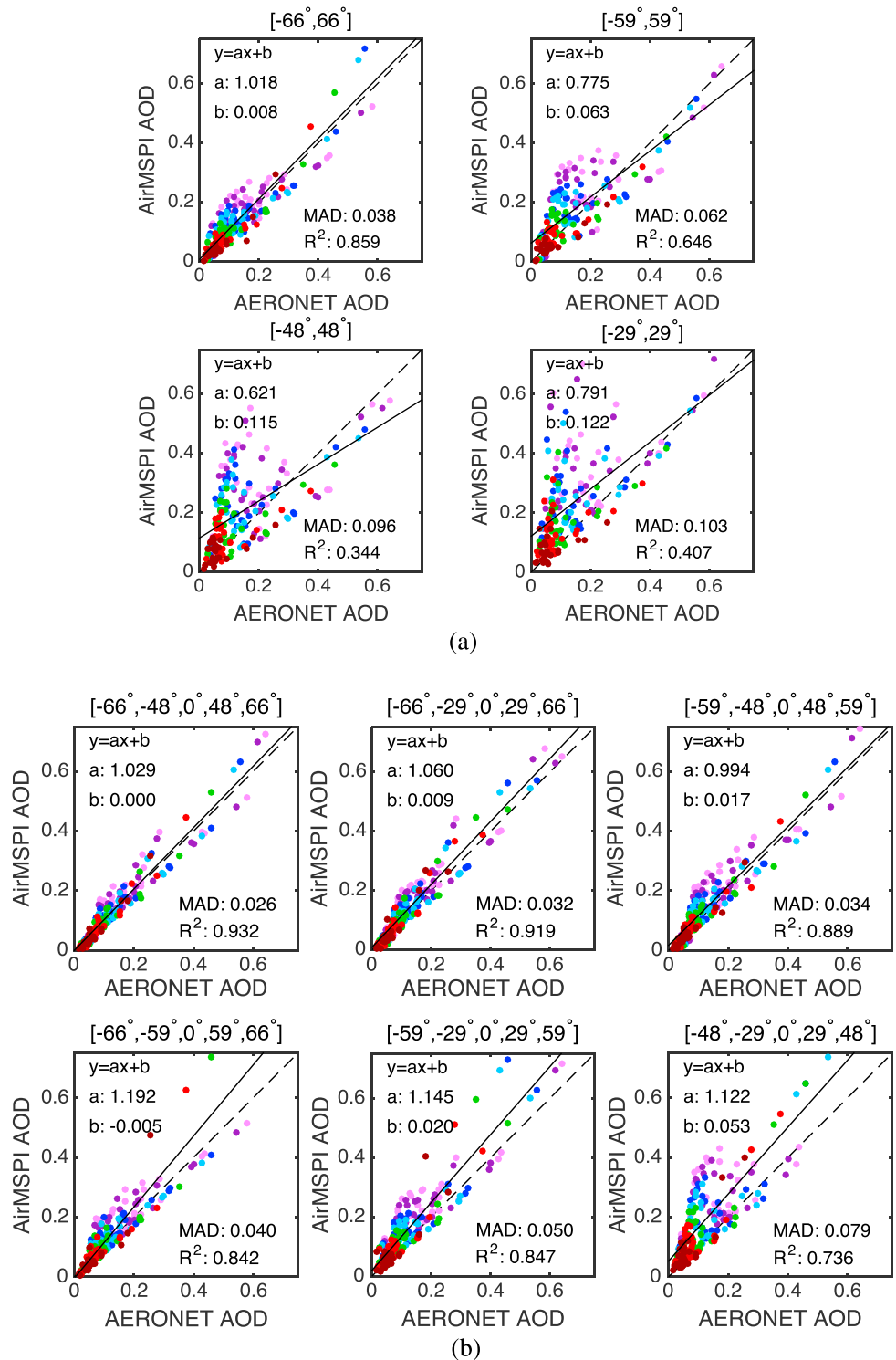


Figure 9. Regression of AirMSPI retrieved AOD against AERONET measured values using different combinations of (a) two-viewing angle and (b) five-viewing angle retrievals. The results for seven AirMSPI spectral bands are plotted in different colors: pink (355 nm), purple (380 nm), dark blue (445 nm), light blue (470 nm), green (555 nm), red (660 nm), and brown (865 nm). As indicated in the subtitle, the results from two-angle combinations ($-66^\circ, +66^\circ$), ($-59^\circ, +59^\circ$), ($-48^\circ, +48^\circ$), and ($-30^\circ, +30^\circ$) are plotted in Figure 9a (top left), Figure 9a (top right), Figure 9a (bottom left), and Figure 9a (bottom right), respectively. The results from five-angle combinations ($0^\circ, \pm 48^\circ, \pm 66^\circ$), ($0^\circ, \pm 29^\circ, \pm 66^\circ$), ($0^\circ, \pm 48^\circ, \pm 59^\circ$), ($0^\circ, \pm 59^\circ, \pm 66^\circ$), ($0^\circ, \pm 29^\circ, \pm 59^\circ$), and ($0^\circ, \pm 29^\circ, \pm 48^\circ$) are plotted in Figure 9b (top left), Figure 9b (top middle), Figure 9b (top right), Figure 9b (bottom left), Figure 9b (bottom middle), and Figure 9b (bottom right), respectively.

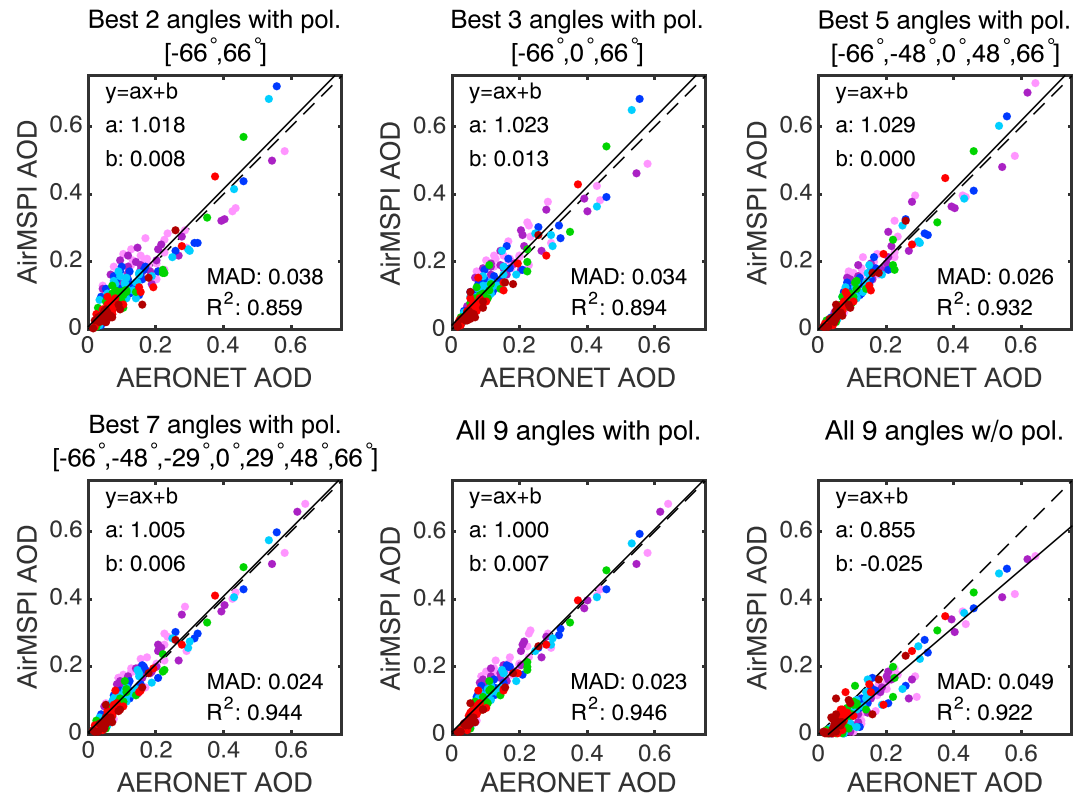


Figure 10. Regression of AirMSPI retrieved AOD against AERONET measured values using different numbers of view angles. For a given number of viewing angles, only the results from the best angular set indicated in a panel title are demonstrated. As described in Figure 9, different colors are assigned to the results for seven AirMSPI spectral bands. The retrievals use observations from (top left) two angles, (top middle) three angles, (top right) five angles, (bottom left) seven angles, and (bottom middle) nine angles, with polarization data at 470, 660, and 865 nm included in the retrievals. The nine-angle-based retrieval without polarization (indicated as “w/o pol.” in the title) is shown in Figure 10 (bottom right).

(bottom middle and right) for AOD and SSA, respectively. Without polarization, MAD of AOD increases. An even larger impact is found for SSA, as its MAD increases from 0.03 to 0.07. Further comparisons of aerosol optical and microphysical properties to AERONET reference data (not demonstrated here) show that the AOD and SSA accuracy gain from using polarization is mainly achieved by reducing the retrieval error of the imaginary part of aerosol refractive index from 6×10^{-3} to 4×10^{-3} . However, it should be noted that it is more advantageous to use (l, q, u) than to use (l, Q, U) in the retrievals. Retrieval tests show that MAD of AOD is 0.037 when using (l, Q, U) , worse than its counterpart 0.023 when using (l, q, u) . Moreover, MAD of SSA is 0.061 when using (l, Q, U) , compared with only 0.033 when using (l, q, u) . This is due to the fact that q and u are only subject to DOLP uncertainty via $\sigma_q = \sigma_u = \sigma_{\text{DOLP}}$, while Q and U are subject to both radiance and DOLP uncertainties via $\sigma_Q = [I^2\sigma_q^2 + q^2(I\delta_i)^2]^{1/2}$ and $\sigma_U = [I^2\sigma_u^2 + u^2(I\delta_i)^2]^{1/2}$.

5.4. Benefits of Temporal Constraints

Under stable weather conditions, surface reflectance and polarization properties within a short interval of time (~days) usually exhibit only small changes. Temporal constraints can thus be imposed on the surface BRDF and pBRDF to constrain the surface retrieval. When a target is visited multiple times by a sensor with different viewing and azimuth angles and the Sun is at different positions in the sky, the surface reflection is better characterized than if independent retrievals are performed for each visit. This in turn should improve aerosol retrieval quality. AirMSPI data provide the opportunity to assess the benefits of target revisits. For example, the Bakersfield site was visited at four different times on 5, 7, and 8 July 2016 during the ImpACT-PM campaign (cf. the geometries of solar incidence and viewing in Figure 12a). To assess the

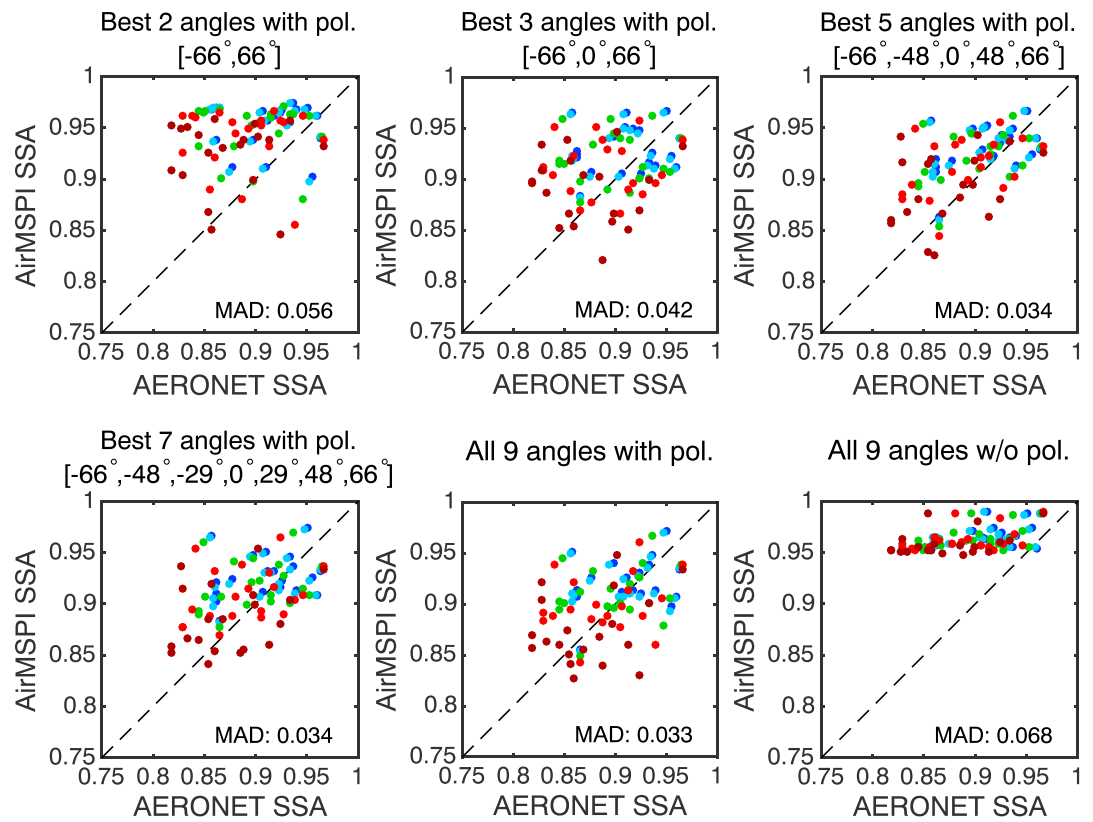


Figure 11. Regression of AirMSPI retrieved SSA against AERONET values using different number of viewing angles. Colors are the same as those in Figure 9, and retrieval conditions are the same as those in Figure 10. In the title of Figure 11 (bottom right), “w/o pol.” means “without polarization.”

benefits of these target revisits, we compare retrievals with and without the imposition of temporal constraints on surface reflectance. The pixels revisited during all four overpasses were used for retrieval. The retrieved surface albedo is compared in Figure 12b, which indicates a reduced spread when temporal constraints are imposed on variations of surface reflection. The improved surface characterization enables a better decoupling of the aerosol signal from the surface contribution. As a result, the AOD retrieval accuracy improves as well, as indicated in Figure 12c. Together with the observations from Figures 10 and 11, we see that either increasing the number of view angles during a single overpass or combining data from multiple visits is effective at reducing retrieval biases. Depending on the characteristics of the sensor and the target revisit strategy, either or both options can be utilized to enhance aerosol retrieval accuracy.

6. Summary

We have developed a multipatch optimization approach for coupled retrieval of aerosol properties and surface reflection over land and tested the algorithm using AirMSPI data. The retrieval error analysis is formulated by accounting for instrumental and modeling errors, as well as for multiple types of physical constraints that help improve the retrieval accuracy and stability by smoothing (a) the spectral variation of aerosol optical properties and a set of parameters describing the surface BRDF and pBRDF; (b) the spatial variation of aerosol parameters across neighboring image pixels; and (c) temporal variations of surface reflection properties. To enhance forward modeling and Jacobian evaluation efficiency, a multilayer model is established for the coupled atmosphere-surface system. Markov chain and doubling methods are used to calculate RT in the aerosol/Rayleigh mixed and pure Rayleigh layer, respectively. The local fields are then coupled by the use of an adding strategy to determine the RT field at the sensor altitude. To enhance retrieval efficiency, the

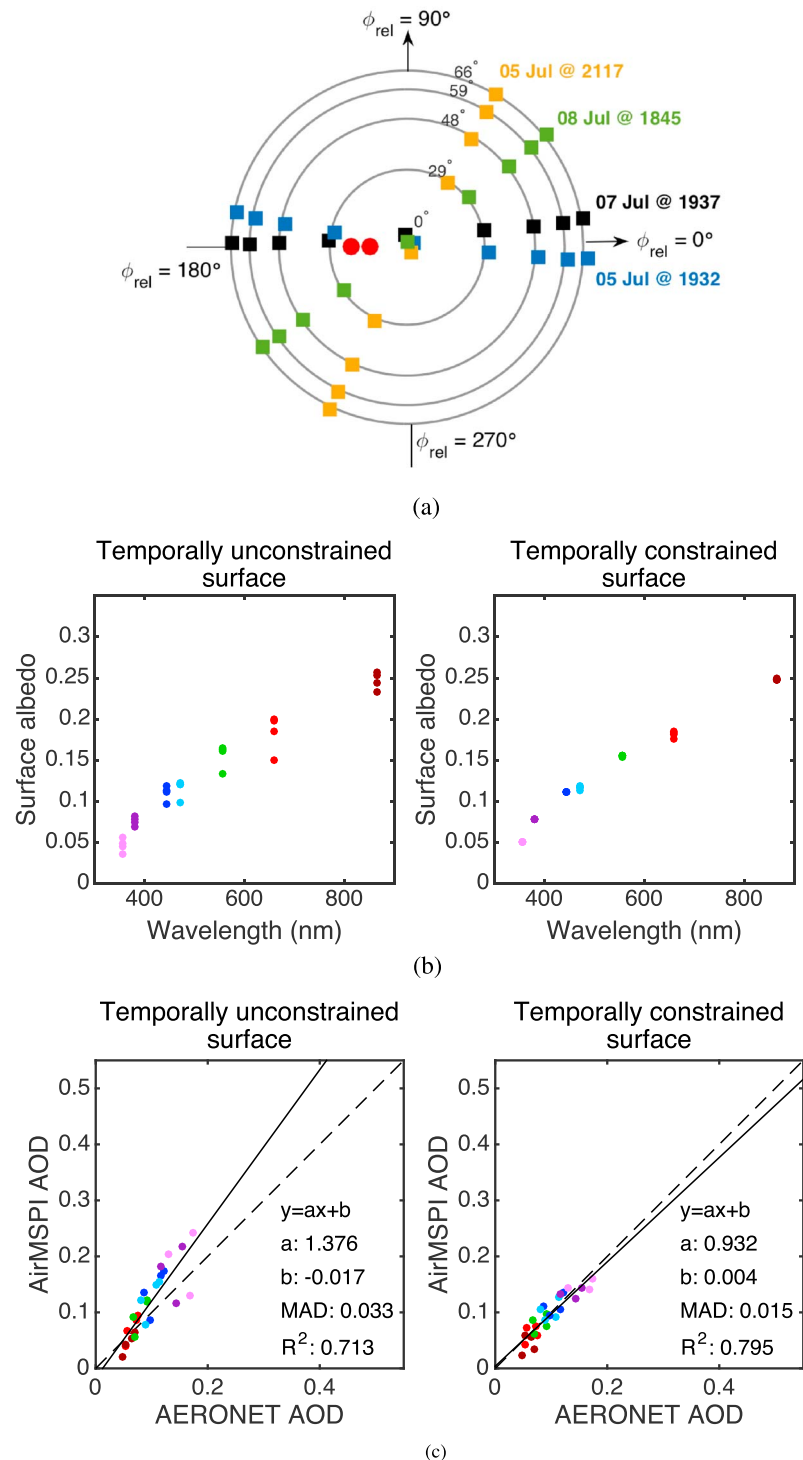


Figure 12. (a) Sun and viewing geometries of four AirMSPI visits over the Bakersfield AERONET site during 5–8 July 2016. For simplicity, the geometries for one image patch are illustrated here. The red dots indicate the solar zenith angle, θ_0 , which had values of 13.9°, 14.0°, 21.0°, and 20.9°. The viewing geometries corresponding to the relative azimuthal angles $\phi_{rel} = \phi_v - \phi_0$ for the four overpasses of about 5°, 170°, 60°, and 40° are marked in black, blue, dark yellow, and green, respectively. (b) Retrieved surface albedo of the single patch from the four overpasses (left) without and (right) with imposition of temporal smoothness constraints on variations of surface reflection. Colors are the same as those specified in Figure 9. Nine-angle polarimetric observations of the pixels revisited during all four overpasses are used for retrieval. (c) Comparison of retrieved AOD from the four overpasses (left) without and (right) with temporal smoothness constraints on variations of surface reflection.

local RT fields for different layers are stored and reused as long as they are not changed during a Jacobian evaluation process.

The retrieval methodology was validated by comparing aerosol retrievals from 27 AirMSPI data sets acquired between 2012 and 2016 with collocated aerosol reference data reported by AERONET. Mean absolute differences between AirMSPI and AERONET retrievals are found to be ~ 0.023 and 0.033 for AOD and SSA, respectively. A strong dependence of retrieval accuracy on the number of viewing angles and angular combinations is found, particularly when the number of view angles is less than five. The AOD accuracy is not significantly improved at greater than five angles. Omitting polarimetry increases the retrieval errors to ~ 0.049 and ~ 0.068 for AOD and SSA, respectively. Using constraints on the temporal variation of surface reflectance improves the aerosol retrieval accuracy, indicating the importance of target revisits especially when the number of viewing angles is insufficient to disentangle the surface and aerosol contributions to the TOA signals. While the algorithm described in this paper has been applied to AirMSPI, it is adaptable to observations by other multispectral, multiangular, and polarimetric instruments on aircraft and satellite platforms. Moreover, although the optimization approach established in this paper uses observations only, it can also be informed with the aerosol spatial distribution/microphysical properties and/or surface reflectance by climatology and chemical transport models via the a priori term or the first guess of the solution (cf. formalism in section 4.1). Some recent studies have been made on combining satellite observations and chemical transport models to further retrieve global aerosol sources or to determine aerosol species amount as well as their microphysical and optical properties [cf. Dubovik et al., 2008; Drury et al., 2008; Wang et al., 2010, among others]. This is our next step of algorithm development for AirMSPI and for the newly selected spaceborne instrument Multi-Angle Imager for Aerosols [Liu and Diner, 2017] under the NASA Earth-Venture-Instrument-3 program.

Acknowledgments

We are grateful to Michael A. Bull, Michael J. Garay, Veljko M. Jovanovic, Brian E. Rheingans, Irina N. Tkatcheva, and Mick Tosca of JPL for their support of AirMSPI's participation in the PODEX, SEAC⁴RS, CalWater-2, and ImpACT-PM field campaigns and for AirMSPI data acquisition and processing. The data used for retrieval test are available at NASA Atmospheric Science Data Center (<https://eosweb.larc.nasa.gov/>). We also thank Otto Hasekamp of SRON, Netherland for helpful discussions on investigating optimal viewing angles for aerosol remote sensing and Marcin Witek of JPL for an extra validation of AirMSPI retrieval using MISR AOD product. This work was performed at the Jet Propulsion Laboratory, California Institute of Technology under contract with the National Aeronautics and Space Administration.

References

- Cahalan, R. F., W. Ridgway, W. J. Wiscombe, T. L. Bell, and J. B. Snider (1994), The albedo of fractal stratocumulus clouds, *J. Atmos. Sci.*, *51*, 2434–2455, doi:10.1175/1520-0469(1994)051<2434:TAOFSC>2.0.CO;2.
- Cairns, B., E. E. Russell, and L. D. Travis (1999), The research scanning polarimeter: Calibration and ground-based measurements, in *Proc. SPIE, Polarization: Measurement, Analysis, and Remote Sensing II*, vol. 3754, 186 pp., Denver, Colo., doi:10.1117/12.366329.
- de Haan, J. F., P. B. Bosma, and J. W. Hovenier (1987), The adding method for multiple scattering calculations of polarized light, *Astron. Astrophys.*, *181*, 371–391.
- Deschamps, P. Y., F. M. Bréon, M. Leroy, A. Podaire, A. Bricaud, J. C. Buriez, and G. Sèze (1994), The POLDER mission: Instrument characteristics and scientific objectives, *IEEE Trans. Geosci. Remote Sens.*, *32*, 598–615, doi:10.1109/36.297978.
- Diner, D. J., et al. (1998), Multi-angle Imaging SpectroRadiometer (MISR) instrument description and experiment overview, *IEEE Trans. Geosci. Remote Sens.*, *36*, 1072–1087, doi:10.1109/36.700992.
- Diner, D. J., A. Davis, B. Hancock, G. Gutt, R. A. Chipman, and B. Cairns (2007), Dual-photoelastic-modulator-based polarimetric imaging concept for aerosol remote sensing, *Appl. Opt.*, *46*, 8428–8445, doi:10.1364/AO.46.008428.
- Diner, D. J., R. A. Hodos, A. B. Davis, M. J. Garay, J. V. Martonchik, S. V. Sanghavi, P. von Allmen, A. A. Kokhanovsky, and P. W. Zhai (2011), An optimized approach for aerosol retrievals using simulated MISR radiances, *Atmos. Res.*, *116*, 1–14, doi:10.1016/j.atmosres.2011.05.020.
- Diner, D. J., et al. (2013), The Airborne Multiangle SpectroPolarimetric Imager (AirMSPI): A new tool for aerosol and cloud remote sensing, *Atmos. Meas. Tech.*, *6*, 2007–2025, doi:10.5194/amt-6-2007-2013.
- Drury, E., D. J. Jacob, J. Wang, R. J. D. Spurr, and K. Chance (2008), Improved algorithm for MODIS satellite retrievals of aerosol optical depths over western North America, *J. Geophys. Res.*, *113*, D16204, doi:10.1029/2007JD009573.
- Dubovik, O. (2004), Optimization of numerical inversion in photopolarimetric remote sensing, in *Photopolarimetry in Remote Sensing*, edited by G. Videen, Y. Yatskiv, and M. Mishchenko, pp. 65–106, Kluwer Acad., Dordrecht, Netherlands.
- Dubovik, O., A. Smirnov, B. N. Holben, M. D. King, Y. J. Kaufman, T. F. Eck, and I. Slutsker (2000), Accuracy assessments of aerosol optical properties retrieved from aerosol robotic network (AERONET) Sun and sky radiance measurements, *J. Geophys. Res.*, *105*(D8), 9791–9806, doi:10.1029/2000JD900040.
- Dubovik, O., et al. (2006), Application of spheroid models to account for aerosol particle nonsphericity in remote sensing of desert dust, *J. Geophys. Res.*, *111*(D11), D11208, doi:10.1029/2005JD006619.
- Dubovik, O., T. Lapyonok, Y. J. Kaufman, M. Chin, P. Ginoux, R. A. Kahn, and A. Sinyuk (2008), Retrieving global aerosol sources from satellites using inverse modeling, *Atmos. Chem. Phys.*, *8*, 209–250, doi:10.5194/acp-8-209-2008.
- Dubovik, O., M. Herman, A. Holdak, T. Lapyonok, D. Tanré, J. L. Deuzé, F. Ducos, A. Sinyuk, and A. Lopatin (2011), Statistically optimized inversion algorithm for enhanced retrieval of aerosol properties from spectral multi-angle polarimetric satellite observations, *Atmos. Meas. Tech.*, *4*, 975–1018, doi:10.5194/amt-4-975-2011.
- Esposito, L. W. (1979), An “adding” algorithm for the Markov chain formalism for radiation transfer, *Astrophys. J.*, *233*, 661–663.
- Esposito, L. W., and L. L. House (1978), Radiative transfer calculated from a Markov chain formalism, *Astrophys. J.*, *219*, 1058–1067.
- Evans, K. F., and G. L. Stephens (1991), A new polarized atmospheric radiative transfer model, *J. Quant. Spectrosc. Radiat. Transfer*, *46*, 413–423, doi:10.1016/0022-4073(91)90043-P.
- Hansen, J. E. (1971), Multiple scattering of polarized light in planetary atmospheres. Part II. Sunlight reflected by terrestrial water clouds, *J. Atmos. Sci.*, *28*, 1400–1426, doi:10.1175/1520-0469(1971)028<1400:MSOPLI>2.0.CO;2.
- Hasekamp, O. P. (2010), Capability of multi-viewing-angle photo-polarimetric measurements for the simultaneous retrieval of aerosol and cloud properties, *Atmos. Meas. Tech.*, *3*, 839–851, doi:10.5194/amt-3-839-2010.

- Hasekamp, O. P., and J. Landgraf (2007), Retrieval of aerosol properties over land surfaces: Capabilities of multiple-viewing-angle intensity and polarization measurements, *Appl. Opt.*, *46*, 3332–3344, doi:10.1364/AO.46.003332.
- Hovenier, J. W. (1969), Symmetry relationships for scattering of polarized light in a slab of randomly oriented particles, *J. Atmos. Sci.*, *26*, 488–499.
- Kahn, R. A., B. J. Gaitley, M. J. Garay, D. J. Diner, T. F. Eck, A. Smirnov, and B. N. Holben (2010), Multiangle Imaging Spectroradiometer global aerosol product assessment by comparison with the Aerosol Robotic Network, *J. Geophys. Res.*, *115*, D23209, doi:10.1029/2010JD014601.
- Kahn, R. A., and B. J. Gaitley (2015), An analysis of global aerosol type as retrieved by MISR, *J. Geophys. Res. Atmos.*, *120*, 4248–4281, doi:10.1002/2015JD023322.
- King, M. D., Y. J. Kaufman, P. Menzel, and D. Tanrd (1992), Remote sensing of cloud, aerosol, and water vapor properties from the moderate resolution imaging spectrometer (MODIS), *IEEE Trans. Geosci. Remote Sens.*, *30*, 2–27, doi:10.1109/36.124212.
- Kokhanovsky, A. A. (2015), The modern aerosol retrieval algorithms based on the simultaneous measurements of the intensity and polarization of reflected solar light: A review, *Front. Environ. Sci.*, *3*, 4, doi:10.3389/fenvs.2015.00004.
- Lebsock, M. D., T. S. L'Ecuyer, and G. L. Stephens (2007), Information content of near-infrared spaceborne multiangular polarization measurements for aerosol retrievals, *J. Geophys. Res.*, *112*, D14206, doi:10.1029/2007JD008535.
- Litvinov, P., O. Hasekamp, and B. Cairns (2011), Models for surface reflection of radiance and polarized radiance: Comparison with airborne multi-angle photopolarimetric measurements and implications for modeling top-of-atmosphere measurements, *Remote Sens. Environ.*, *115*, 781–792, doi:10.1016/j.rse.2010.11.005.
- Liu, Y., and D. J. Diner (2017), Multi-angle imager for aerosols, *Public Health Rep.*, *132*, 14–17, doi:10.1177/0033354916679983.
- Martins, J. V., R. Fernandez-Borda, L. Sparr, G. Dolgos, R. Espinosa, S. Buczkowski, L. A. Remer, and Z. Zhang (2013), Measurements of polarized light scattering by atmospheric particles with the Passive Aerosol and Cloud Suite (PACS), presented at the Electromagnetic & Light Scattering XIV, Lille, France, 17 June.
- Mishchenko, M. I., and L. D. Travis (1997), Satellite retrieval of aerosol properties over the ocean using polarization as well as intensity of reflected sunlight, *J. Geophys. Res.*, *102*, 16,989–17,013, doi:10.1029/96JD02425.
- Ortega, J. M., and Rheinboldt, W. C. (1970), Iterative solution of nonlinear equations in several variables, Academic Press, New York, London.
- Rahman, H., B. Pinty, and M. M. Verstraete (1993), Coupled surface-atmosphere reflectance (CSAR) model 2. Semiempirical surface model usable with NOAA advanced very high resolution radiometer data, *J. Geophys. Res.*, *98*(D11), 20,791–20,781, doi:10.1029/93JD02072.
- Rietjens, J. H. H., J. M. Smit, G. van Harten, A. Di Noia, A., O. P. Hasekamp, J. de Boer, H. Volten, F. Snik, and C. U. Keller (2015), Accurate spectrally modulating polarimeters for atmospheric aerosol characterization, *Proc. SPIE 9613, Polarization Science and Remote Sensing VII*, vol. 9613, doi:10.1117/12.2188024.
- Salomonson, V. V., W. L. Barnes, P. W. Maymon, H. E. Montgomery, and H. Ostrow (1989), MODIS: Advanced facility instrument for studies of the Earth as a system, *IEEE Trans. Geosci. Remote Sens.*, *27*, 145–153, doi:10.1109/36.20292.
- Stokes, G. G. (1862), On the intensity of the light reflected from or transmitted through a pile of plates, *Proc. R. Soc. London*, *11*, 545–556.
- van de Hulst, H. C. (1963), A new look at multiple scattering, Tech. Rep., Goddard Institute for Space Studies, NASA TM-103044, 81 pp.
- Wang, J., X. Xu, R. Spurr, Y. Wang, and E. Drury (2010), Improved algorithm for MODIS satellite retrievals of aerosol optical thickness over land in dusty atmosphere: Implications for air quality monitoring in China, *Remote Sens. Environ.*, *114*(11), 2575–2583, doi:10.1016/j.rse.2010.05.034.
- Wu, L., O. Hasekamp, B. van Diedenoven, and B. Cairns (2015), Aerosol retrieval from multiangle, multispectral photopolarimetric measurements: Importance of spectral range and angular resolution, *Atmos. Meas. Tech.*, *8*, 2625–2638, doi:10.5194/amt-8-2625-2015.
- Xu, F., A. B. Davis, R. A. West, and L. W. Esposito (2010), Markov chain formalism for polarized light transfer in plane-parallel atmospheres, with numerical comparison to the Monte Carlo method, *Opt. Express*, *19*, 946–967, doi:10.1364/OE.19.000946.
- Xu, F., A. B. Davis, R. A. West, J. V. Martonchik, and D. J. Diner (2011), Markov chain formalism for vector radiative transfer in a plane-parallel atmosphere overlying a polarizing surface, *Opt. Lett.*, *36*, 2083–2085, doi:10.1364/OL.36.002083.
- Xu, F., A. B. Davis, S. V. Suniti, J. V. Martonchik, and D. J. Diner (2012), Linearization of Markov chain formalism for vector radiative transfer in a plane-parallel atmosphere/surface system, *Appl. Opt.*, *51*, 3491–3507, doi:10.1364/AO.51.003491.
- Xu, F., et al. (2016), Joint retrieval of aerosol and water-leaving radiance from multispectral, multiangular and polarimetric measurements over ocean, *Atmos. Meas. Tech.*, *9*, 2877–2907, doi:10.5194/amt-9-2877-2016.
- Xu, X., and J. Wang (2015), Retrieval of aerosol microphysical properties from AERONET photopolarimetric measurements: 1. Information content analysis, *J. Geophys. Res. Atmos.*, *120*, 7059–7078, doi:10.1002/2015JD023108.